
GEOMETRY-AWARE FRAMEWORK FOR DEEP ENERGY METHOD: AN APPLICATION TO STRUCTURAL MECHANICS WITH HYPERELASTIC MATERIALS

A PREPRINT

**Thi Nguyen Khoa Nguyen^{1,2,3}, Thibault Dairay^{1,2}, Raphaël Meunier², Jean Di Stasio²,
Christophe Millet^{1,3}, Mathilde Mougeot^{1,4}**

¹*Universite Paris-Saclay, ENS Paris-Saclay, CNRS, Centre Borelli, Gif-sur-Yvette, 91190 France*

²*Michelin, Centre de Recherche de Ladoux, Cébazat, 63118 France*

³*CEA, DAM, DIF, F-91297 Arpajon, France*

⁴*ENSIIE, Évry-Courcouronnes, 91000 France*

May 7, 2024

ABSTRACT

Physics-Informed Neural Networks (PINNs) have gained considerable interest in diverse engineering domains thanks to their capacity to integrate physical laws into deep learning models. Recently, geometry-aware PINN-based approaches that employ the strong form of underlying physical system equations have been developed with the aim of integrating geometric information into PINNs. Despite ongoing research, the assessment of PINNs in problems with various geometries remains an active area of investigation. In this work, we introduce a novel physics-informed framework named the Geometry-Aware Deep Energy Method (GADEM) for solving structural mechanics problems on different geometries. As the weak form of the physical system equation (or the energy-based approach) has demonstrated clear advantages compared to the strong form for solving solid mechanics problems, GADEM employs the weak form and aims to infer the solution on multiple shapes of geometries. Integrating a geometry-aware framework into an energy-based method results in an effective physics-informed deep learning model in terms of accuracy and computational cost. Different ways to represent the geometric information and to encode the geometric latent vectors are investigated in this work. We introduce a loss function of GADEM which is minimized based on the potential energy of all considered geometries. An adaptive learning method is also employed for the sampling of collocation points to enhance the performance of GADEM. We present some applications of GADEM to solve solid mechanics problems, including a loading simulation of a toy tire involving contact mechanics and large deformation hyperelasticity. The numerical results of this work demonstrate the remarkable capability of GADEM to infer the solution on various and new shapes of geometries using only one trained model.

Keywords Physics-informed neural networks, deep energy method, hyperelastic materials, contact mechanics

1 Introduction

Partial differential equations (PDEs) are widely used to model and analyze physical problems in engineering. Due to the difficulty of obtaining analytical solutions, various numerical methods for solving these equations have been proposed and widely used, such as the finite difference method, finite element method, and finite volume method [Quarteroni and Valli, 2008, Ames, 2014]. However, these schemes remain expensive in practice due to the large number of degrees of freedom (DOFs) required to accurately solve the PDEs [Amsallem, 2010], and a skillful mesh refinement technique is required to enhance the accuracy [De SR Gago et al., 1983]. In the last few years, advances in

deep learning methods have gained much attention in the field of physical modeling. These methods have increasingly been used to study the physics of systems by incorporating physical constraints, which are typically expressed as PDEs, into the models [Yu et al., 2018, Raissi et al., 2019, Rackauckas et al., 2020, Samaniego et al., 2020]. Among these studies, the series of work by Karniadakis' group on Physics-Informed Neural Networks (PINNs) [Raissi et al., 2019, Karniadakis et al., 2021] stands out as an attractive and remarkable approach to solving forward and inverse PDE problems. PINNs use neural networks as approximators and integrate the physical constraints of the systems into the cost function by minimizing the PDE residuals calculated on a set of collocation points (non-supervised points). Thanks to their simplicity and powerful capability when dealing with problems involving PDE or systems of PDEs, PINNs are gaining more and more attention from researchers in engineering fields.

Recently, many studies focused on improving the efficiency of PINNs by using adaptive strategies, such as adaptive activation functions Jagtap et al. [2020b,a, 2022], adaptive weights in the cost function [McClenny and Braga-Neto, 2020, Wang et al., 2020a,b, 2022], and adaptive collocation points during the training [Peng et al., 2022, Daw et al., 2022, Wu et al., 2023, Nguyen et al., 2023]. Besides that, many extensions of PINNs are gradually being developed and improved, whether to overcome the computational limitation or to deal with spectral bias of the neural networks [Kharazmi et al., 2019, Pang et al., 2019, Yang et al., 2021, Jagtap and Karniadakis, 2021, Moseley et al., 2023]. Besides that, the applicability of PINNs has been demonstrated in a wide range of research areas. For example, Chen et al. [2020] applied PINNs for inverse problems in nano-optics and metamaterials, Kissas et al. [2020], Arzani et al. [2021] employed PINNs for the modeling of cardiovascular flows and blood flow, Strelow et al. [2023] applied PINNs to gas transport problems, Shukla et al. [2021] used PINNs to identify polycrystalline nickel material coefficients, Nguyen et al. [2022] applied PINNs in a non-Newtonian fluid thermo-mechanical problem which is used in the rubber calendaring process, Chen et al. [2023] employed a physics informed framework to forecast a tumor growth.

Current efforts also focus on developing convolutional neural networks (CNN) to efficiently learn large-scale spatiotemporal physical fields [Fang, 2021, Ren et al., 2022, Li et al., 2020]. However, these convolutional-based deep learning frameworks require a regular grid for the training points and are not efficient when dealing with irregular geometries. To overcome this challenge, Gao et al. [2021] introduced a physics-informed architecture using convolutional neural networks, which is trainable on a set of geometries, named PhyGeoNet that uses elliptic mapping to transform an irregular physical domain into a regular reference domain. Li et al. [2023] proposed a geometry-aware extension of the Fourier neural operator named Geo-FNO, which deforms the irregular input domain into a uniform latent mesh on which the Fourier transform can be applied. Recently, Serrano et al. [2024] introduced the coordinate-based model for operator learning framework (CORAL), which is based on implicit neural representations and able to learn mappings between functions sampled on irregular meshes, for solving PDEs on general geometries.

As far as computational mechanics is concerned, there has been a growing number of studies that focus on the capability of PINNs to solve problems involving solid mechanics. Haghghat et al. [2021] employed PINNs with the PDE-based approach (strong form of the system) to identify the material parameters in solid mechanics problems. With the same technique, Sahin et al. [2023] utilized PINNs to solve a contact mechanic in linear elasticity. Samaniego et al. [2020], Nguyen-Thanh et al. [2020, 2021] proposed to use the Deep Energy Method (DEM) (a weak form of the system) in the loss function of PINNs to solve linear elasticity and hyperelasticity problems. Fuhg and Bouklas [2022] introduced an extension of DEM named mixed Deep Energy Method (mDEM) that enhances the training capability of the network by taking the stress components as additional outputs. However, this approach requires higher computational resources due to additional input and the computation of the first Piola-Kirchhoff stress tensor. Abueidda et al. [2023] introduced a framework that combined the strong form and the weak form of the system, and employed the coefficient of variation weighting scheme to enhance the accuracy of the model. Chadha et al. [2022] used Bayesian optimization algorithms and random search to identify optimal values for hyperparameters when using DEM. Lee et al. [2024] proposed an extension of DEM designed for multiphysics simulation named adversarial Deep Energy Method (adversarial DEM) for solving saddle point problems with electromechanical coupling. Li et al. [2021] compared the PDE-based approach and the energy-based approach in the problem of predicting the mechanical responses of elastic plates. Throughout these works, the energy-based approach has been demonstrated to be more efficient than the PDE-based approach for solving solid mechanics problems in terms of accuracy and computational resources, as it only requires first-order automated differentiation.

However, one drawback of the classical PINNs and DEM is that the model is capable of inferring the solution on only one configuration, that is, one needs to retrain PINNs or DEM in case dealing with a new geometry. To tackle this issue, Kashefi and Mukerji [2022] proposed a Physics-informed PointNet (PIPNet) that used a point-cloud-based neural network to encode the geometric features so that the model can predict the solution on multiple sets of irregular geometries. With the same purpose, Oldenburg et al. [2022] introduced geometry-aware PINNs (GAPINNs) that used a Variational Autoencoder (VAE) [Kingma et al., 2019] to extract geometric latent vector, and then used this latent vector as input of the neural networks. The PhyGeoNet framework of Gao et al. [2021] is also trainable on a set of geometries and able to infer the solution on new geometries. Recently Cameron et al. [2024] proposed a neural operator architecture

designed to learn PDE solutions based on boundary geometry. This approach does not constrain the geometry to a fixed, finite-dimensional parameterization, and therefore is capable of estimating the PDE solution over a whole new geometry.

In this paper, we introduce a novel framework, which is an extension of GAPINNs that employs deep energy method in the loss function, named the Geometry-Aware Deep Energy Method (GADEM) to infer the solution of structural mechanical problems using the energy-based approach. In the first training phase, different representation techniques, such as spatial coordinates of the objects' boundaries or images of the objects, are employed to represent the geometries. To encode geometric information, parametric encoding (*i.e.* the parameters that control the shapes of geometries, if available) or dimensionality reduction methods are employed. In particular, we invest and compare a linear dimensionality reduction method (Principal Component Analysis [Jolliffe, 2002]), and a non-linear method (Variational Autoencoder) [Kingma et al., 2019], to encode the geometric information into latent vectors. In the second phase, the model uses the geometric latent vectors as additional input for the networks. The Deep Energy Method is utilized during the second phase and we minimize the loss (which is the potential energy of the system) over all the training geometries. We also employ an original adaptive strategy Nguyen et al. [2023] to infer the best location for the training points to enhance the performance of GADEM. We first validate our proposed method on an academic test case with various shapes of geometries and the reference solutions are obtained using the Finite Element Method (FEM). We then consider the problem of contact between a deformable object and a rigid obstacle, which involves additional inequality constraints in the loss function. This application consists of a simplified tire loading simulation that involves different irregular geometries. To the best of our knowledge, this is the first time a physics-informed deep learning framework has been successfully applied to solve a contact mechanics problem involving hyperelastic materials on different geometries. All our results are compared to a reference solution obtained with a finite element solver. The code used in this study is available on the GitHub repository <https://github.com/nguyenkhoa0209/gadem> upon publication.

The following of this paper is organized as follows. In section 2, the mathematical formulation of contact mechanics for hyperelastic materials is introduced. In section 3, the framework of vanilla PINNs and the Deep Energy Method for solving forward problems in contact mechanics are presented. Later in this section, we introduce the Geometry-Aware Deep Energy Method (GADEM) and its formulation. An adaptive training strategy for the energy-based methods is also briefly presented in this section. In section 4, we validate our framework in an academic test case of linear elasticity. We then investigate the performance of GADEM in the tire loading simulation in section 5. Finally, the conclusions and perspectives are summarized in section 6.

2 Contact mechanics for hyperelastic materials

In the following, we consider a contact problem between a deformable body made of hyperelastic material and a rigid obstacle. The body is denoted as Ω in its initial configuration (reference configuration before deformation). Assuming the static case, the function that describes the deformation of the body and maps it from the initial configuration into the actual configuration is denoted by Φ . The actual configuration is then denoted by $\Phi(\Omega)$. For a point of the deformable body, we denote \mathbf{X} the position vector in the initial configuration, and \mathbf{x} the position vector in the actual configuration. Then the relation between two positions is given by $\mathbf{x} = \Phi(\mathbf{X}) = \mathbf{X} + \mathbf{u}(\mathbf{X})$ where \mathbf{u} denotes the displacement vector.

The boundary of the object at the initial configuration $\partial\Omega$ can be represented as $\partial\Omega = \partial\Omega_D \cup \partial\Omega_N \cup \partial\Omega_C$, where $\partial\Omega_D$ denotes the Dirichlet boundary where displacements are applied, $\partial\Omega_N$ denotes the Neumann boundary where the pressure is applied, and $\partial\Omega_C$ denotes the boundary where there is potential contact with other rigid obstacle. We consider the boundary value problem with the governing equations as follows:

$$\operatorname{div} \mathbf{P} + \mathbf{f}_b = \mathbf{0} \text{ on } \Omega \quad (1)$$

$$\mathbf{u} = \mathbf{u}^* \text{ on } \partial\Omega_D \quad (2)$$

$$\mathbf{P} \cdot \mathbf{N} = \mathbf{t}^* \text{ on } \partial\Omega_N \quad (3)$$

where \mathbf{P} denotes the first Piola-Kirchhoff stress tensor, \mathbf{f}_b denotes the density force on the body, \mathbf{N} denotes the outward normal vector, and $\mathbf{u}^*, \mathbf{t}^*$ denotes the reference values on Dirichlet boundary and Neumann boundary, respectively. The deformation gradient tensor which measures the deformation of the body Ω is defined as:

$$\mathbf{F} = \nabla_{\mathbf{X}} \Phi(\mathbf{X}) = \mathbf{I} + \nabla_{\mathbf{X}} \mathbf{u}$$

To describe the behavior of hyperelastic materials, the strain energy function Ψ can be used to show a relation between the stress tensors and the displacement field. The first Piola-Kirchhoff stress tensor can be given as follows:

$$\mathbf{P} = \frac{\partial \Psi}{\partial \mathbf{F}}$$

In this work, we focus on the Saint-Venant Kirchhoff hyperelastic model, a generalization of linear elasticity. The strain energy in this model is given by:

$$\Psi = \lambda \text{tr}^2(\mathbf{E})\mathbf{I} + \mu \text{tr}(\mathbf{E}^2)$$

where λ and μ are the Lamé constants, and $\mathbf{E} = \frac{1}{2}(\mathbf{F}^T \mathbf{F} - \mathbf{I})$ is Green-Lagrange tensor.

The potential energy of the system, which is at minimum in the equilibrium state, is given by:

$$\Pi(\phi) = \int_{\Omega} \Psi dV - \left(\int_{\Omega} \mathbf{f}_b \cdot \phi dV + \int_{\Omega_N} \mathbf{t}^* \cdot \phi dA \right) \quad (4)$$

where $\phi \in \mathcal{H}$ is a trial function, \mathcal{H} denotes the space of trial functions (admissible functions) [Fortin and Garon, 2011]. In (4), The term $\int_{\Omega} \Psi dV$ represents the internal energy, and the term $\left(\int_{\Omega} \mathbf{f}_b \cdot \phi dV + \int_{\Omega_N} \mathbf{t}^* \cdot \phi dA \right)$ represents the external energy.

Solving the system of PDEs (1),(2),(3) is referred to as solving the strong form of the system, while minimizing the potential energy (4) is referred to as solving the weak form of the system. The weak form has a clear advantage compared to the strong form in that it only requires first-order differentiation, and thus reduces a huge amount of computational resources. In this work, we focus on solving the mechanical problems using the weak formulation. The calculation of the integral is discussed in more detail in section 3.2.

Next, we present the additional conditions when there is frictionless contact between the body Ω and a rigid obstacle. On the potential contact boundary Ω_C , the three conditions representing unilateral contact (also known as Signorini conditions) are given by:

$$u_n \leq g \quad (5)$$

$$P_n \leq 0 \quad (6)$$

$$P_n(u_n - g) = 0 \quad (7)$$

The initial gap g is calculated by $g = (\mathbf{X}_0 - \mathbf{X}) \cdot \mathbf{n}$ where \mathbf{X}_0 is the corresponding projection of \mathbf{X} onto the rigid obstacle. The normal component of u is given by $u_n = \mathbf{u} \cdot \mathbf{n}$ where \mathbf{n} is the outward normal vector of the object in the actual configuration, and the normal component of first Piola-Kirchhoff stress tensor is given by $P_n = (\mathbf{P} \cdot \mathbf{N}) \cdot \mathbf{n}$. Inequation 5 indicates that no penetration can occur, that is, the gap between the body and the obstacle can only be positive or zero. Inequation 6 forces the non-adhesive stress in the contact zone. Equation 7 indicates that when there is contact (the gap is zero, $u_n = g$), the normal stress is different than zero ($P_n < 0$), and when there is no contact (the gap is positive, $u_n < g$), the normal stress is identical to zero. The contact conditions can be integrated into the potential energy as follows:

$$\Pi(\phi) = \int_{\Omega} \Psi dV - \left(\int_{\Omega} \mathbf{f}_b \cdot \phi dV + \int_{\Omega_N} \mathbf{t}^* \cdot \phi dA \right) - \int_{\Omega_C} P_n(u_n - g)$$

where $P_n \in \mathcal{P}$, and $\mathcal{P} = \{q \in \mathcal{H}_C | q \leq 0\}$ is the space of trial functions. Interested readers may refer to the work of Papadopoulos and Taylor [1992] and Khenous et al. [2006] for further theoretical formulations. In this work, we choose to impose these contact constraints as a strong formulation. More details are described in section 3.1.

3 Methodology

In this section, the framework of the vanilla Physics-informed neural networks (PINNs) for solving contact mechanics problems is presented. The Deep Energy Method (DEM) based on PINNs is then illustrated. Later in this section, the Geometry-aware Deep Energy Method (GADEM) is introduced.

3.1 Physics-informed neural networks

The general framework of PINNs for solving problems involving PDE or systems of PDEs can be found in Raissi et al. [2019], Karniadakis et al. [2021]. Here we present the framework of PINNs for solving forward problems for contact mechanics, which involves solving the systems of equations (1),(2),(3) with the constraints (5),(6),(7).

In the conventional framework of PINNs [Raissi et al., 2019], the displacement \mathbf{u} is approximated by a fully connected feedforward neural network \mathcal{NN} , which takes the spatial coordinate \mathbf{X} (positions of the object at initial configuration) as inputs and the solution \mathbf{u} as output. This can be represented as follows:

$$\mathbf{u} \approx \hat{\mathbf{u}} = \mathcal{NN}(\mathbf{X}, \theta)$$

where \mathcal{NN} denotes the neural networks, $\hat{\mathbf{u}}$ denotes the prediction value for the displacement and $\boldsymbol{\theta}$ denotes the trainable parameters of the neural network. The parameters of the neural network are trained by minimizing the cost function L :

$$L(\boldsymbol{\theta}) = L_{pde}(\boldsymbol{\theta}) + L_{bc_D}(\boldsymbol{\theta}) + L_{bc_N}(\boldsymbol{\theta}) + L_{contact}(\boldsymbol{\theta}) \quad (8)$$

where the terms L_{pde} , L_{bc_D} , L_{bc_N} , and $L_{contact}$ penalize the loss in the residual of the PDE, the Dirichlet boundary condition, the Neumann boundary condition, and the contact conditions respectively, which can be represented as follow:

$$\begin{aligned} L_{pde}(\boldsymbol{\theta}) &= \frac{1}{N_{pde}} \sum_{i=1}^{N_{pde}} \|\text{div} \hat{\mathbf{P}}(\mathbf{X}_i) + (\mathbf{f}_b)_i\|^2 \\ L_{bc_D}(\boldsymbol{\theta}) &= \frac{w_{bc_D}}{N_{bc_D}} \sum_{i=1}^{N_{bc_D}} |\hat{\mathbf{u}}_i - \mathbf{u}_i^*|^2 \\ L_{bc_N}(\boldsymbol{\theta}) &= \frac{w_{bc_N}}{N_{bc_N}} \sum_{i=1}^{N_{bc_N}} |\hat{\mathbf{P}}(\mathbf{X}_i) \hat{\mathbf{N}}(\mathbf{X}_i) - \mathbf{t}_i^*|^2 \end{aligned}$$

where N_{bc_D} , N_{bc_N} denote the numbers of training points for the Dirichlet and Neumann boundary condition, and measurements, respectively, and N_{pde} denotes the number of residual points (or collocation points or unsupervised points) of the PDE. w_{bc_D} , w_{bc_N} are the weight coefficients for different loss terms, which are used to adjust the contribution of each term to the cost function. For the contact conditions which involve inequalities, there are different ways to enforce these constraints. Lu et al. [2021b] proposed to use soft constraints, penalty method, and augmented Lagrangian method to enforce the inequalities as hard constraints into the loss function. Sahin et al. [2023] proposed the sign-based method, sigmoid-based method, and Fischer-Burmeister function to enforce these constraints. The details and performance of each method can be found in the cited references. In this work, we present the results of using the Fischer-Burmeister function as our preliminary results suggest that this method performs better than the others in terms of accuracy and robustness. We use the Fischer-Burmeister function as follows:

$$\varphi(a, b) = a + b - \sqrt{a^2 + b^2}$$

which has the property that $\varphi(a, b) = 0 \Leftrightarrow a \geq 0, b \geq 0, ab = 0$. Then the contact constraints (5),(6),(7) can be implemented as follows:

$$L_{contact}(\boldsymbol{\theta}) = \frac{w_c}{N_c} \sum_{i=1}^{N_c} |g(\mathbf{X}_i) - u_n(\mathbf{X}_i) - P_n(\mathbf{X}_i) + \sqrt{(g(\mathbf{X}_i) - u_n(\mathbf{X}_i))^2 + P_n(\mathbf{X}_i)^2}|^2 \quad (9)$$

where N_c denotes the number of training points on the potential contact zone, w_c is the weight coefficient for the contact loss term. The weight coefficients w_{bc_D} , w_{bc_N} , w_c can be either pre-specified before the training or tuned during the training. To construct the residual loss L_{pde} , automatic differentiation (AD) [Baydin et al., 2018] is used to compute the partial derivatives of the output $\hat{\mathbf{u}}$ of the network with respect to the inputs \mathbf{X} .

3.2 Deep energy method based on PINNs

Samaniego et al. [2020], Nguyen-Thanh et al. [2021] introduced the Deep Energy Method (DEM) to infer the solution of mechanical problems by minimizing the loss function which is not based on residual equations but on the potential energy of the system. More precisely, the loss function in DEM is formulated as follows:

$$L(\boldsymbol{\theta}) = \Pi(\hat{\phi}) + L_{contact}(\boldsymbol{\theta}) = \int_{\Omega} \hat{\Psi} dV - \int_{\Omega} \mathbf{f}_b \cdot \hat{\phi} dV - \int_{\Omega_N} \mathbf{t}^* \cdot \hat{\phi} dA + L_{contact}(\boldsymbol{\theta})$$

where $\hat{\phi}$, $\hat{\Psi}$ denote the predictions of the neural networks for ϕ and Ψ , respectively. The trial function is expressed as $\hat{\phi} = \hat{\mathbf{u}} + \mathbf{X}$, where the prediction for the displacement $\hat{\mathbf{u}}$ satisfies the Dirichlet condition *a priori*. To this end, we can multiply the output of the neural networks by a distance function to the Dirichlet boundary Ω_D . The interested readers may refer to the work of Berg and Nyström [2018], Liu et al. [2019] for the general formulations. The detail of the distance function used in this work is given in section 5.1. We note however that we can enforce the boundary conditions softly as in the classical PINNs by minimizing the mean square error (MSE) between the prediction and the solution on these boundaries. The formulation of the loss $L_{contact}$ for contact constraints remains the same as (9).

To approximate the integrals, there exist various numerical methods such as the trapezoidal rule Simpson’s rule, Gaussian quadrature, and the Monte-Carlo method. In this work, we employ the Monte Carlo method as this method allows the training points to be randomly generated over the entire domain, which is efficient in case of irregular geometries. The loss function now becomes as follows:

$$L(\boldsymbol{\theta}) \approx \frac{1}{N} \sum_{i=1}^N \hat{\Psi}(\mathbf{X}_i)V - \frac{1}{N} \sum_{i=1}^N (\mathbf{f}_b)_i \cdot \hat{\boldsymbol{\phi}}_i V - \frac{1}{N_N} \sum_{i=1}^{N_N} (\mathbf{t}^*)_i \cdot \hat{\boldsymbol{\phi}}_i A + L_{contact}(\boldsymbol{\theta})$$

where N, N_N denotes the number of training points in the domain and on the Neumann boundary, respectively, V denotes the volume (in 3D) or area (in 2D) of the object, and A denotes the area (in 3D) or length (in 2D) of the potential contact zone.

3.3 Geometry-aware deep energy method

With the purpose of building a model that is able to predict the solution on different geometries, we need a model that takes into account the geometric information. Oldenburg et al. [2022] proposed to use a variational autoencoder [Kingma et al., 2019] on boundary (spatial) coordinates of the objects to infer the latent representation of each geometric shape. Inspired by this work, we separate the training into two phases. In the first phase, we use geometric encoding methods to extract the geometric information into latent vectors. In the second phase, the latent vector is considered as the input of the DEM network. The loss function is now defined by the sum of the loss functions of the classical DEM in each geometry. In this work, we employ either the discretized spatial coordinates of the objects’ boundaries or images of the objects to represent the geometries. We also investigate and compare the performance of the model using different geometric encoding methods: parametric encoding (that is, the parameters that control the shapes of geometries, if available) and different reduction methods: Principal Component Analysis (PCA) [Jolliffe, 2002] and Variational Autoencoder (VAE). In our framework, during the second phase, we rely on the Deep Energy Method to formulate the loss function, that is, the potential of the system is minimized. In the following, we refer to this framework as the Geometry-aware Deep Energy Method (GADEM).

For the training during the first phase, if the geometric parameters are available, we take them directly as input of the model for the second phase. If not, the spatial coordinates of the objects’ boundaries or the images of the objects are used to represent the geometries. More precisely, each geometry is represented by its boundary spatial coordinates or its black-and-white image represented by a matrix of 0s and 1s. These data are taken as the input of the PCA and VAE. For the VAE, we use 1D (for spatial coordinates) or 2D (for images) convolution layers, followed by fully connected layers to predict the mean $\boldsymbol{\mu}_X$ and variance $\boldsymbol{\sigma}_X$ of the posterior distribution. In the decoder, the latent vector is taken as input, and fully connected layers are employed to reconstruct the boundaries. The details of the architecture of the VAE are given in the appendix A.

After the training of reduction methods, the geometric latent vector \mathbf{z} (that is the geometric parameters (if available) or the latent space of the PCA, or the output of the encoder of the VAE) is taken as an input of GADEM.

$$\hat{\mathbf{u}} = \mathcal{N}(\mathbf{X}, \mathbf{z}, \boldsymbol{\theta})$$

The final loss function of GADEM is the sum of the PINNs loss of all the training geometries. Since we employ the Deep Energy Method, the loss function can be represented as follows:

$$L_{GADEM}(\boldsymbol{\theta}) = \sum_{j=1}^{N_G} \left(\frac{1}{N^j} \sum_{i=1}^{N^j} \hat{\Psi}(\mathbf{X}_i^j)V^j - \frac{1}{N^j} \sum_{i=1}^{N^j} (\mathbf{f}_b)_i^j \cdot \hat{\boldsymbol{\phi}}_i^j V^j - \frac{1}{N_N^j} \sum_{i=1}^{N_N^j} (\mathbf{t}^*)_i^j \cdot \hat{\boldsymbol{\phi}}_i^j A^j + L_{contact}^j(\boldsymbol{\theta}) \right)$$

The architecture of GADEM and the training configurations are given in detail in each application. In the following, for the sake of clarity, we denote different approaches of GADEM as follows:

- Parametric: explicit parametric encoding. This approach is straightforward to implement in cases where the parameters that control the shape of geometry are available.
- PCA-Coord: spatial coordinates for the geometric representation and PCA for the encoding. This approach can be employed when we dispose of the spatial coordinates of the objects’ boundaries. The training of PCA is fast (compared to the VAE), however, the PCA can only learn the linear representations. The performance using the PCA may decrease when dealing with complex geometries.
- VAE-Coord: spatial coordinates for the geometric representation and VAE for the encoding. As PCA-Coord, this approach can be employed when the spatial coordinates of the objects’ boundaries are available. As the VAE can learn non-linear representation, it offers greater flexibility than PCA when dealing with complex geometries.

- PCA-Image: images for the geometric representation and PCA for the encoding. This approach can be employed when the objects' images are available. The advantages and drawbacks of using PCA are discussed above.
- VAE-Image: images for the geometric representation and VAE for the encoding. This approach can be employed when the objects' images are available. The advantages and drawbacks of using the VAE are discussed above.

The configuration and architecture of the neural networks are specified in each test case. The detailed configuration and performance of the PCA and VAE can be found in the appendix.

3.4 Adaptive learning strategy for collocation points for energy-based methods

In PINNs and DEM, the loss for PDE residuals or the potential energy is computed on a set of collocation points (non-supervised points). In the literature on vanilla PINNs, the training collocation points are often fixed during the training process [Raissi et al., 2019, Karniadakis et al., 2021]. It has been shown that the location of these collocation points has a great impact on the performance of PINNs [Lu et al., 2021a, Daw et al., 2022, Nguyen et al., 2022]. Recently, a considerable amount of work has also developed adaptive re-sampling techniques for the collocation points during the training [Peng et al., 2022, Daw et al., 2022, Zeng et al., 2022, Wu et al., 2023]. Nguyen et al. [2023] proposed the Fixed-Budget Online Adaptive Learning (FBOAL) strategy that decomposes the domain into smaller sub-domains, then adds and removes the collocation points based on the PDEs residuals so that the local extremum of the PDEs residuals can be quickly captured by the method given a constant budget of collocation points. The authors also show that the method can be utilized in parametric cases, where the PDE parameters may vary. In this work, we employ FBOAL to improve the performance of GADEM. The main idea of FBOAL is to add and remove collocation points that yield the largest and the smallest PDE residuals on the sub-domains during the training. After the training, the number of training points remains the same as the initial training configuration. We note that, when parametric encoding or latent vectors are considered as additional inputs of the training, FBOAL can relocate the training points adaptively following the parametric encoding or the latent vectors. The details of the method can be found in the reference [Nguyen et al., 2023]. In this work, we use a simplified version of FBOAL (i.e., we do not effectuate the domain decomposition step) to infer adaptively the position of collocation points for the energy-based methods (DEM or GADEM). We recall the loss function of DEM:

$$L(\theta) = \int_{\Omega} \hat{\Psi} dV - \int_{\Omega} \mathbf{f}_b \cdot \hat{\phi} dV - \int_{\Omega_N} \mathbf{t}^* \cdot \hat{\phi} dA + L_{contact}(\theta)$$

In this loss function, the training points are from three different sets Ω , Ω_N , Ω_C , and on each set, different independent quantities are minimized. Thus we can treat these training sets independently. For the sake of simplicity, in the following, we describe the FBOAL algorithm on the domain Ω . Our goal is to minimize the following quantity on Ω :

$$\int_{\Omega} \hat{\Psi} dV - \int_{\Omega} \mathbf{f}_b \cdot \hat{\phi} dV = \int_{\Omega} (\hat{\Psi} - \mathbf{f}_b \cdot \hat{\phi}) dV \approx \frac{1}{N} \sum_{i=1}^N (\hat{\Psi}(\mathbf{X}_i) - (\mathbf{f}_b)_i \cdot \hat{\phi}_i) V = \frac{1}{N} \sum_{i=1}^N e(\mathbf{X}_i) V$$

where we denote the quantity $e(\mathbf{X}_i) = \hat{\Psi}(\mathbf{X}_i) - (\mathbf{f}_b)_i \cdot \hat{\phi}_i$. The simplified FBOAL algorithm effectuated on Ω is described as follows:

Procedure 1 Simplified Fixed-Budget Online Adaptive Learning (FBOAL)

Require: The number of added and removed points m , the period of resampling k

- 1: Generate the set \mathcal{C} of collocation points inside the domain Ω .
 - 2: Train the networks for K iterations.
 - 3: **repeat**
 - 4: Generate a new set \mathcal{C}' of random points inside the domain Ω .
 - 5: Compute the quantity $e(\mathbf{X}'_i)$ at all points in the set \mathcal{C}' and sort \mathbf{X}'_i in decreasing order.
 - 6: Compute the quantity $e(\mathbf{X}_i)$ at all points in the set \mathcal{C} and sort \mathbf{X}_i in decreasing order.
 - 7: Update $\mathcal{C} \leftarrow \mathcal{C} \setminus \{\mathbf{X}_i\}_{i=m}^N \cup \{\mathbf{X}'_i\}_{i=1}^m$
 - 8: Train the networks for k iterations.
 - 9: **until** The maximum number of iterations is reached.
-

A similar approach can be effectuated on Ω_N, Ω_C . For GADEM, we apply the same approach as described above, except that now we calculate the quantity $e(\mathbf{X}_i)$ over all the training geometries.

4 Numerical results on an academic test case

Before tackling a complex problem involving hyperelastic material and contact constraints, we validate GADEM in an academic case of linear elasticity without contact. The goal is to assess and compare the performance of different approaches for geometric representation and encoding in GADEM. More precisely, we investigate the displacement of a beam whose geometry depends on five parameters l, d, l_1, p_1, p_2 , and the right side of the beam is shaped by two parameters p_1, p_2 . The left side of the beam is clamped and the right side is subjected to a traction $\vec{P} = (0, -1)N$. The beam is made of a homogeneous, isotropic material with Young's modulus $E = 1000N/m^2$, and Poisson's ratio $\nu = 0.3$. The reference solution is calculated using the Finite Element Method (FEM) and is obtained by Fenics [Logg et al., 2012]. To evaluate the accuracy of the prediction, we calculate the relative \mathcal{L}^2 error defined as follows:

$$\epsilon_u = \frac{\|\mathbf{u} - \hat{\mathbf{u}}\|_2}{\|\mathbf{u}\|_2}$$

where \mathbf{u} denotes the reference solution for the displacement and $\hat{\mathbf{u}}$ is the corresponding prediction.

For the training geometry data set, we use a Latin Hypercube Sampling (LHS) to generate 50 geometries where the right side of the beam is of the shape $p_1 \sin(p_2 x)$ and 50 geometries where the right side of the beam is of the shape $p_1 x^{p_2}$. Figures 1a and 1b show an example of geometries in each training set together with the problem setup. The training values of the parameters are detailed in Table 1.

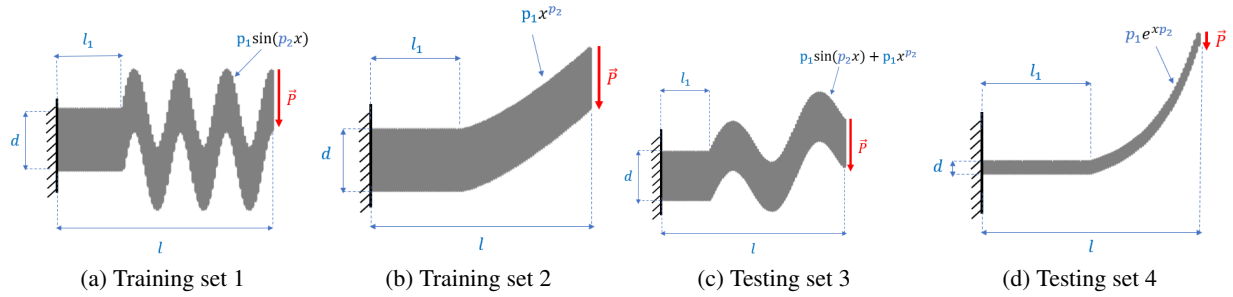


Figure 1: Visualization of the training and testing geometries and problem setup.

With the purpose of testing the capability of GADEM in various types of geometries, for the testing geometry set, we use LHS to generate four types of testing. In the first testing set, we generate the geometries with the same shapes as the training set, and the parameters in the same intervals as the training. In the second testing set, we generate the geometries with the same shapes as the training set, however, the parameters are in different intervals than the ones used for training. In the third testing set, we generate the parameters in the same intervals as the training, however, the geometries are now of the shape $p_1 \sin(p_2 x) + p_1 x^{p_2}$. In the fourth set, we generate the parameters in the same intervals as the training, however, the geometries are now of the shape $p_1 \exp(p_2 x)$. We see that the geometries in the third set are new, but still a linear combination of the training set. The geometries in the fourth set are completely new to the training. Figures 1c and 1d show an example of geometries in the third and the fourth testing set. The values of the parameters are detailed in Table 1.

	Nb. geometries	Shape	Interval of parameters l, d, p_1, p_2, p
Train	50	$p_1 \sin(p_2 x)$	$[4, 12], [1, 3], [1, 2], [0.5, 1.5], [0.25, 0.5]$
	50	$p_1 x^{p_2}$	$[4, 12], [1, 3], [0.1, 1], [1, 1.5], [0.25, 0.5]$
Test 1	10	$p_1 \sin(p_2 x)$	$[4, 12], [1, 3], [1, 2], [0.5, 1.5], [0.25, 0.5]$
	10	$p_1 x^{p_2}$	$[4, 12], [1, 3], [0.1, 1], [1, 1.5], [0.25, 0.5]$
Test 2	10	$p_1 \sin(p_2 x)$	$[12, 14], [3, 4], [2, 2.5], [0.25, 0.5], [0.5, 0.6]$
	10	$p_1 x^{p_2}$	$[2, 4], [0.5, 1], [0.05, 0.1], [1.5, 2], [0.1, 0.25]$
Test 3	20	$p_1 \sin(p_2 x) + p_1 x^{p_2}$	$[4, 12], [1, 3], [1, 2], [0.5, 1.5], [0.25, 0.5]$
Test 4	20	$p_1 \exp(p_2 x)$	$[4, 12], [1, 3], [1, 2], [0.5, 1.5], [0.25, 0.5]$

Table 1: Configuration for the geometries in training and testing sets.

First training phase (i.e. extracting the geometric latent vector): For the training of GADEM during the first phase, to represent the geometries using spatial coordinates, we dispose of $N_b = 400$ regular points on the boundaries of each

geometry. To represent the geometries using images, we dispose of an image of resolution 200×200 . To compare fairly different approaches of geometric encoding, the number of kept components in the PCA and the size of the latent vectors in the VAE are fixed $k_z = 5$, which is equal to the number of geometric parameters (l, d, l_1, p_1, p_2) . The architecture of the VAE is specified in the appendix A.1. The visualization of the latent vectors is also provided in the appendix A.2.

Second training phase: During the second phase of GADEM, for each geometry, we randomly generate $N_j = 5000$ collocation points. Fully connected layers are employed with 5 layers and 100 neurons per layer, and the hyperbolic tangent is used as an activation function. This architecture is inspired by the work of Raissi et al. [2019], allowing a good balance between the network representation capacity and the computational costs based on our preliminary results. To minimize the loss function, we adopt L-BFGS optimizer with the number of maximum epochs equal to 5×10^4 . A distance function is used so that the prediction for the displacement satisfies the Dirichlet boundary conditions *a priori*. As the left side of the beams is clamped, that is $\mathbf{u} = \mathbf{0}$ on $\partial\Omega_D = \{\mathbf{X} = (x, y) | x = 0\}$, the output of the neural networks is of the form: $\hat{\mathbf{u}} = x\mathcal{NN}(\mathbf{X}, \mathbf{z}, \boldsymbol{\theta})$.

Figure 2 shows the visualization of the reference solution and the predictions of GADEM for some examples on the training set and testing sets. We see that all approaches of GADEM give good predictions for the displacements in the training set. For the testing sets, the parametric encoding, PCA-Coord, and VAE-Coord are able to provide accurate predictions, while PCA-Image and VAE-Coord give less accurate predictions.

To evaluate the accuracy of GADEM, we choose testing points for each geometry. More precisely, for each geometry, we choose $N_{test} = 10000$ points and evaluate the error of the prediction on these testing points. Figures 3 and 4 illustrate more precisely the performance of all approaches in terms of accuracy evaluated on testing points. Figure 3 shows the box plots of relative \mathcal{L}^2 errors of the prediction of GADEM for all the geometries in the training geometry data set. We see that all the approaches of GADEM are able to give good accuracies for the prediction. The PCA-Coord and VAE-Coord approaches give nearly the same performance and even better than the explicit parametric encodings, whereas the PCA-Image and VAE-Image give the least accurate predictions. Figure 4 shows the box plots of relative \mathcal{L}^2 errors of the prediction of GADEM for all the geometries in the testing geometry data sets. In general, we see that the parametric encoding always gives good performance for the predictions. The methods that use spatial coordinates (PCA-Coord and VAE-Coord) outperform the ones using images (PCA-Image and VAE-Image). More precisely, in the first test (where the geometries have the same shapes and learning intervals as the training set), the VAE-Coord approach provides the most accurate and robust predictions, followed by PCA-Coord and parametric encoding. In the second test (where the geometries have the same shapes as the training set but different learning intervals), the parametric encoding and VAE-Coord provide good and nearly the same performances. In the third and fourth tests (where the geometries have different shapes from the training), the parametric encoding provides the best results, followed by PCA-Coord and VAE-Coord approaches.

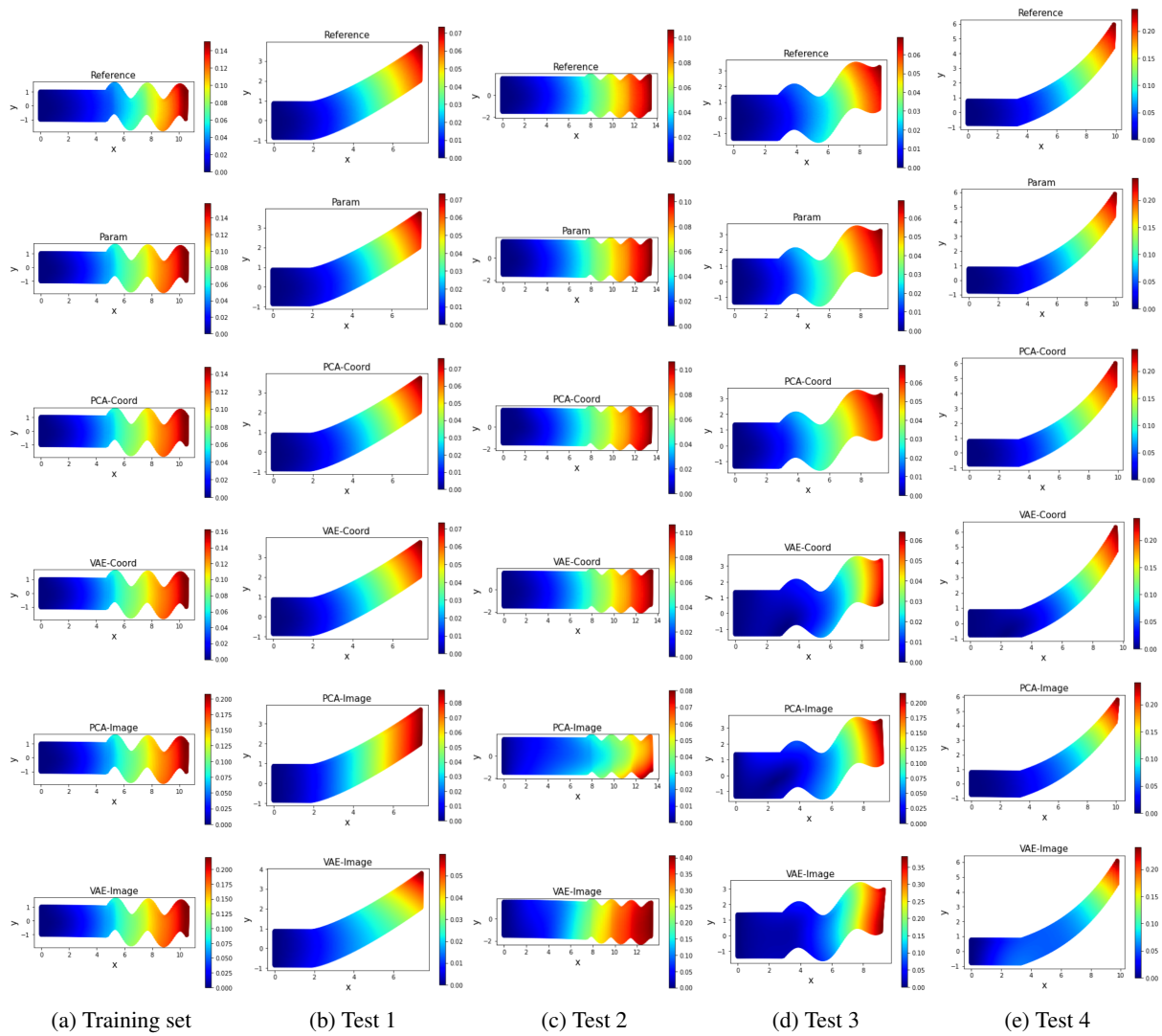


Figure 2: Reference solution and prediction by GADEM on training and testing sets.

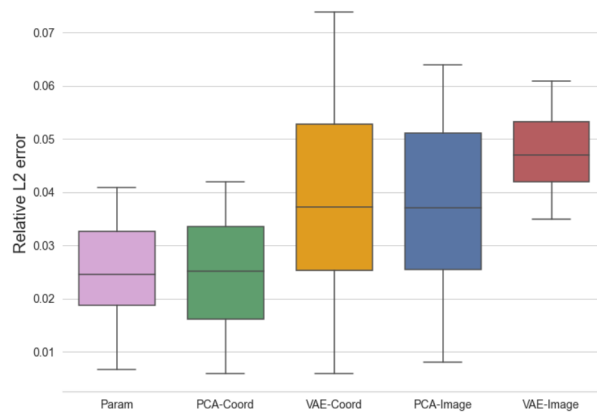


Figure 3: Performance for all geometries in the training data set.

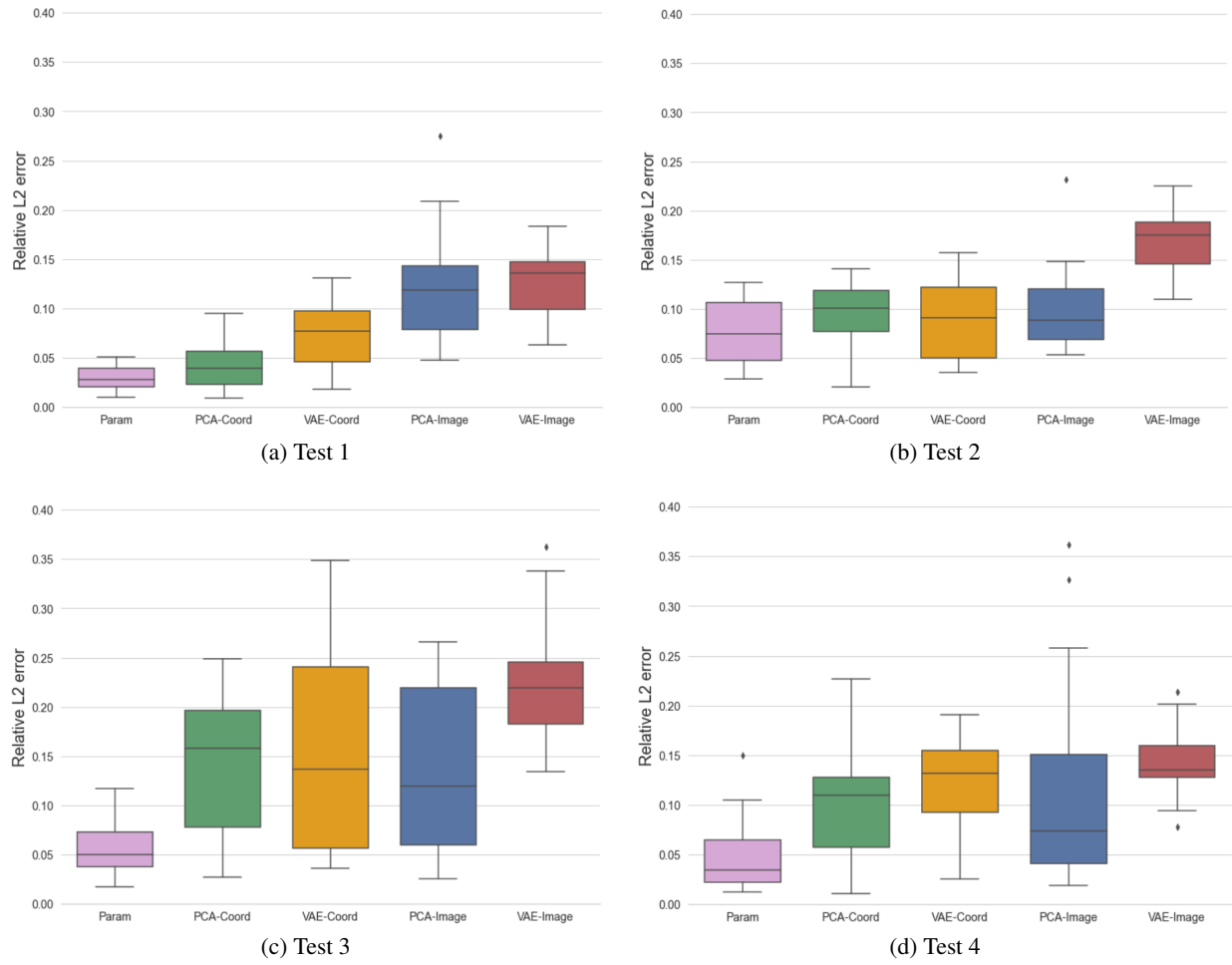


Figure 4: Performance on the testing data sets.

Table 2 shows the relative \mathcal{L}^2 errors (average results of all the geometries) of all considered approaches on the training and testing sets. The good results (errors smaller than 10%) are highlighted. The same conclusion can be drawn from the training and testing sets: parametric encoding always provides good performance in terms of accuracy, and using the spatial coordinates to represent the geometries is better than using the images. We note that the accuracy of GADeM can be further improved by increasing the number of training collocation points, or using adaptive training methods for the activation function or the weights in the loss function Jagtap et al. [2020b], McClenny and Braga-Neto [2020]. In this work, we use FBOAL to infer adaptively the training collocation points to enhance the performance of GADeM.

		Params	PCA-Coord	VAE-Coord	PCA-Image	VAE-Image
ϵ_{train}	W/o (*)	2.52e-2±9.37e-3	2.46e-2±1.00e-2	3.85e-2±1.83e-2	3.79e-2±1.59e-2	4.74e-2±6.85e-3
	With (*)	1.67e-2±1.16e-2	1.83e-2±1.48e-2	2.78e-2±2.13e-2	2.54e-2±2.91e-2	3.89e-2±2.61e-2
ϵ_{test_1}	W/o (*)	2.99e-2±1.26e-2	4.30e-2±2.62e-2	7.31e-2±3.51e-2	1.27e-1±6.71e-2	1.26e-1±3.05e-2
	With (*)	2.21e-2±1.75e-2	3.72e-2±3.88e-2	6.58e-2±4.67e-2	1.16e-1±7.63e-2	1.19e-1±4.12e-2
ϵ_{test_2}	W/o (*)	7.63e-2±2.24e-2	9.43e-2±3.59e-2	9.03e-2±4.36e-2	1.05e-1±5.09e-2	1.71e-1±3.45e-2
	With (*)	7.08e-2±2.31e-2	8.65e-2±4.38e-2	8.42e-2±5.73e-2	9.81e-1±6.96e-2	1.64e-1±3.88e-2
ϵ_{test_3}	W/o (*)	5.68e-2±2.75e-2	1.43e-1±7.03e-2	1.55e-1±1.08e-1	1.36e-1±8.36e-2	2.24e-1±6.09e-2
	With (*)	4.97e-2±3.28e-2	1.35e-1±7.47e-2	1.48e-1±1.39e-2	1.28e-1±8.93e-2	2.19e-1±6.51e-2
ϵ_{test_4}	W/o (*)	4.99e-2±3.74e-2	1.00e-1±5.73e-2	1.21e-1±4.61e-2	1.19e-1±1.08e-1	1.43e-1±3.56e-2
	With (*)	4.31e-2±3.45e-2	9.52e-2±4.19e-2	1.15e-1±5.10e-2	1.10e-1±3.40e-2	1.38e-1±4.34e-1

 Table 2: Relative \mathcal{L}^2 error of different approaches of GADeM with and without using FBOAL (*).

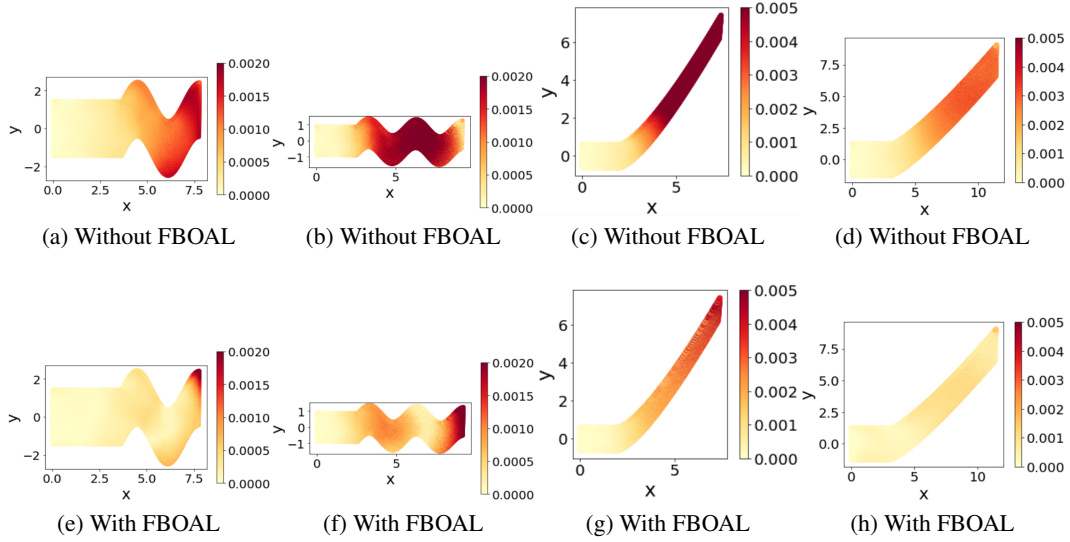


Figure 5: Visualization of the absolute error between the reference solution and GADEM with parametric encoding for beams in the training set: (a-d) without using FBOAL, (e-h) with using FBOAL on corresponding beams.

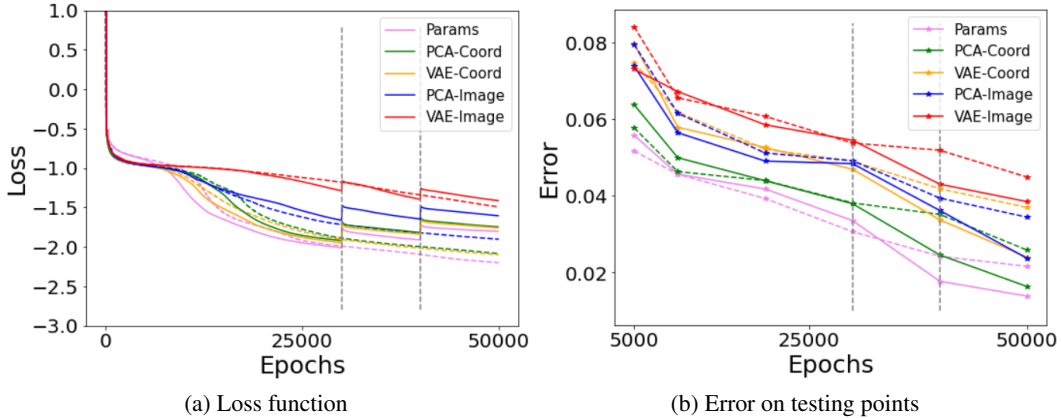


Figure 6: Loss function during the training process and the relative \mathcal{L}^2 errors on the testing points (average results of all geometries) produced by GADEM without FBOAL (dashed lines) and GADEM with FBOAL (solid lines). The gray lines indicate the instances where FBOAL effectuates the resampling.

For the sake of comparison, we use the same initial training configuration as described above, that is, for each geometry, we dispose of $N_j = 5000$ randomly generated collocation points. This leads to the number of collocation points $N = 100 \times 5000 = 500000$ points. For the training of FBOAL, we first train the network for $K = 30000$ iterations, and then after every $k = 10000$ iterations, we add and remove $m = 1\% \times N = 5000$ points based on the energy quantity to minimize for all the training geometries. We note that the hyperparameters m and k can be tuned to obtain the best performance of FBOAL. The study of these hyperparameters is presented in the work of Nguyen et al. [2023]. Here we choose the values of m and k based on the conclusion of this work.

Figure 5 illustrates the absolute error between the reference solution and GADEM with parametric encoding for tires in the training set with and without using FBOAL. From this figure and Table 2, we can see that FBOAL helps to improve significantly the accuracy of GADEM on the training geometry set. The same conclusion can be drawn for the testing geometry sets. Figure 6 shows the loss function during the training by all GADEM approaches and the relative \mathcal{L}^2 errors of the prediction over all geometries on the testing points. We see that when FBOAL effectuates the resampling (*i.e.* the positions of the training collocations points are modified), there are jumps in the loss functions. Thus the loss functions produced by GADEM with FBOAL are less well minimized than the ones produced by GADEM without

FBOAL (Figure 6a). However, the prediction errors on the testing points are significantly reduced by using GADEM with FBOAL (Figure 6b).

5 Application to toy tire loading simulation

5.1 Problem configuration and formulation

During the initial phase of tire design, static loading simulations are a crucial step for the designer to determine the basic properties of the tire. The modeling of the tire loading step is a challenging task especially when dealing with different shapes of tire geometries, different materials, and potentially 3D effects. For the sake of simplicity, the goal of the present study is only to model the 2D displacement of toy tires composed of hyperelastic materials (rubber in our case). An illustration of the tire before and after loading is shown in Figure 7.

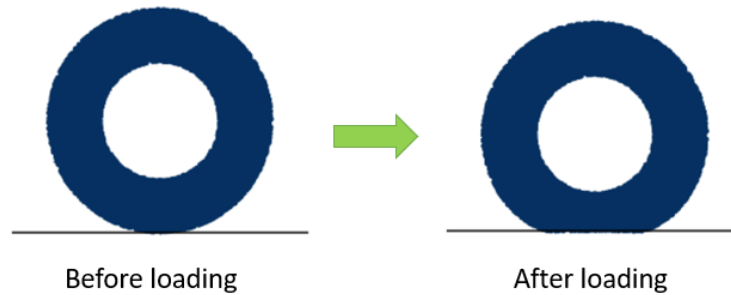


Figure 7: Sketch of a tire before and after loading.

The tires are made of rubber with a Young modulus $E = 21.10^6 Pa$ and a Poisson's ratio $\nu = 0.3$. We assume that the tires follow the Saint-Venant Kirchhoff hyperelastic model. The physical domain of interest together with the geometrical configuration of the study are presented in Figure 8. The tires are supposed to be in contact with rigid ground. A Dirichlet boundary condition $\mathbf{u}_D = (0, -0.01)m$ is imposed on the rim of the tires (the inner circles). A Neumann boundary $\mathbf{P} \cdot \mathbf{N} = 0$ is applied on the outer boundary of the tires. The potential contact boundaries with the floor can be taken as the lower outer boundaries (shown as green lines in Figure 8). We suppose that there is no body force applied to the tires.

$$\Pi(\phi) = \int_{\Omega} \Psi dV = \int_{\Omega} \lambda \text{tr}^2(\mathbf{E}) \mathbf{I} + \mu \text{tr}(\mathbf{E}^2) dV$$

where the Lamé constants are given as $\lambda = \frac{\nu E}{(1 + \nu)(1 - 2\nu)}$, and $\mu = \frac{E}{2(1 + \nu)}$.

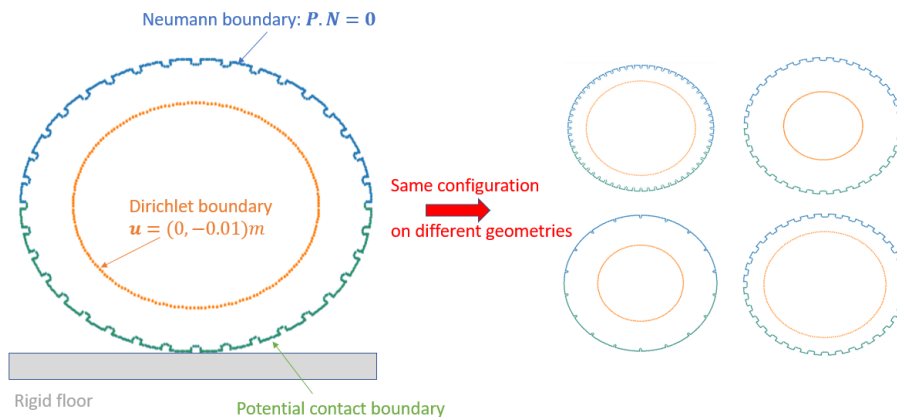


Figure 8: Sketch of the 2D configuration and example of some learning geometries considered in the present study.

To generate reference High-Fidelity (HF) solutions of the displacement field, we use the finite element solver GetFEM Renard and Pommier [2007]. Again, to evaluate the performance of the model in predicting the displacement, we calculate the relative \mathcal{L}^2 error defined as follows:

$$\epsilon_{\mathbf{u}} = \frac{\|\mathbf{u} - \hat{\mathbf{u}}\|_2}{\|\mathbf{u}\|_2}$$

where \mathbf{u} denotes the reference solution for the displacement and $\hat{\mathbf{u}}$ is the corresponding prediction. In our work, the errors are evaluated on the finite element mesh. The number of nodes on the mesh varies with different geometries, from 11934 points to 32636 points. The GetFEM solver gives us high-fidelity solutions on the finite-element mesh.

5.2 Numerical results

5.2.1 Extracting the geometric latent vector

We generate a set of 55 geometries for the tires. In this set, there are 5 main groups of geometries, which are distinguished by the radius of the inner and the outer boundaries. In each group, the geometries are distinguished by the grooves. The data set is divided into a training set of 33 geometries in four groups, and two testing sets of 22 geometries: the first testing set includes 11 geometries in the same groups as the training set, and the second one includes 11 geometries in a different group from the training groups (out-of-distribution (OOD) testing set). A visualization for the training set and testing set in a reduced space can be found in Figure 9. Since our goal is to compare different approaches to represent and encode the geometries, in the following, we choose the fifth group of tires as the OOD testing set. The impact of choosing another group as the OOD testing is presented in the appendix B.

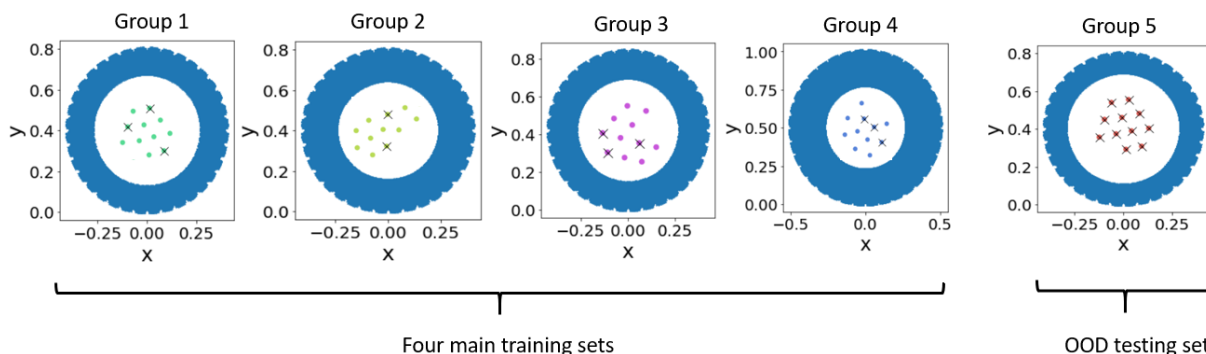


Figure 9: Illustration of the training and OOD testing sets. Inside each training set, we also choose some tires for testing. The testing tires are denoted by the 'x' symbol.

To represent the geometries using spatial coordinates, we dispose of $N_b = 1400$ points on the boundaries, which are composed of 1200 points of the outer boundary, and 200 points of the inner boundary. To further improve the performance of the reduction methods, we consider employing the reduction methods on only a small part of the tires, which represents the grooves. Then the final latent vector will be composed of the latent vectors produced by the reduction methods on the grooves, and the radius of the inner and outer boundary of the tires. Figure 10 illustrates explicitly this procedure on a training tire.

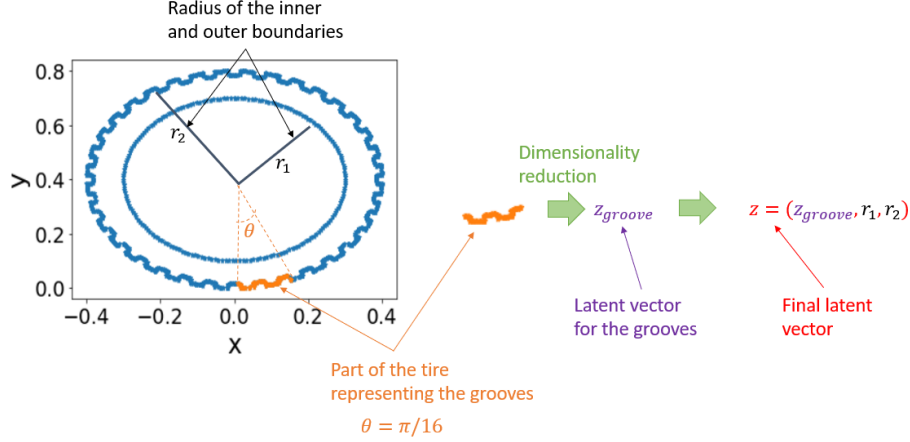


Figure 10: Illustration of the procedure that employs the reduction methods on a part of the tires representing the grooves. r_1, r_2 denotes the radius of the inner and outer boundaries, respectively. Part of the tire representing the grooves is controlled by an angle $\theta = \pi/16$.

To represent the geometries using images, we dispose of an image of resolution 200×200 that represents the boundaries for each geometry. The PCA and VAE are employed to build the latent vectors that represent the geometric features.

- PCA-Coord: the latent vector is of the form $z = (z_{groove}, r_1, r_2)$. We only effectuate PCA on the part that represents the grooves. The number of kept components of the PCA is fixed as $k_{z_{groove}} = 3$, or $k_z = 5$. Before effectuating the PCA, the input data are centered.
- VAE-Coord: the latent vector is of the form $z = (z_{groove}, r_1, r_2)$. We only effectuate VAE on the part that represents the grooves. The size of the latent vector of the VAE is fixed as $k_{z_{groove}} = 3$, or $k_z = 5$.
- PCA-Image: the latent vector is of the form $z = z_{tire}$. We effectuate the PCA on the images that represent the boundaries of the tires. The number of kept components of the PCA is fixed as $k_z = 5$. Before effectuating the PCA, the input data are centered.
- VAE-Image: the latent vector is of the form $z = z_{tire}$. We effectuate the VAE on the images that represent the boundaries of the tires. The size of the latent vector of the VAE is fixed as $k_z = 5$.

More details of the configuration and the performance of the PCA and VAE, and also the visualization of the latent vectors can be found in the appendix A.1 and A.3.

	PCA-Coord	VAE-Coord	PCA-Image	VAE-Image
Training time	3.54e-3 ± 8.59e-4	1.93e+2 ± 6.07e+1	1.01e-1 ± 7.74e-3	7.66e+2 ± 5.14e+1

Table 3: Training time (or calculation time in second) during the first phase of GADEM approaches.

Table 3 shows the training time during the first phase of all GADEM approaches, *i.e.* the calculation time for the reduction methods to extract geometric latent vectors. We see that with PCA, we gain a huge amount of calculation time compared to the VAE. When these methods are effectuated on the spatial coordinates that represent the grooves, we save even better training time.

5.2.2 Performance on tire loading simulation

The extracted geometric latent vector z is taken into the input of GADEM. As we use the Deep Energy Method in the loss function, it is preferred that the prediction of the displacement satisfies the Dirichlet boundary condition *a priori* $u_D = (0, -0.01)m$. To do this, we multiply the output of the neural network by a distance function to this boundary (which is in our case the inner boundary of the tire), that is:

$$\hat{u} = \mathcal{NN}(\mathbf{X}, z_r, \theta) \cdot \text{dist}(\mathbf{X}, bc_D) + u_D$$

where bc_D represents the Dirichlet boundary. As the inner boundary of the tires is perfect circles, the distance function can be formulated as:

$$\text{dist}(\mathbf{X}, bc_D) = (X_x - c_x)^2/r^2 + (X_y - c_y)^2/r^2 - 1$$

where X_x, X_y are the horizontal and vertical components of \mathbf{X} , (c_x, c_y) represents the coordinates of the center of the circle, and r is the radius of the circle. In the loss function, the potential energy is minimized with the contact constraints for all geometries:

$$\begin{aligned} L_{GADEM}(\boldsymbol{\theta}) &= \sum_{j=1}^{N_G} \left(\Pi(\hat{\phi}^j) + L_{contact}^j(\boldsymbol{\theta}) \right) = \sum_{j=1}^{N_G} \left(\int_{\Omega^j} \hat{\Psi}^j dV^j + L_{contact}^j(\boldsymbol{\theta}) \right) \\ &= \sum_{j=1}^{N_G} \left(\frac{1}{N^j} \sum_{i=1}^{N^j} \hat{\Psi}(\mathbf{X}_i^j) V^j + L_{contact}^j(\boldsymbol{\theta}) \right) \end{aligned}$$

where the loss contact $L_{contact}^j$ is defined as (9).

For the training, on each geometry, we take $N_j = 2500$ collocation points, which are randomly generated inside the domain, to minimize the energy. For the contact constraints, we take $N_c = 600$ points on the potential contact boundary of each geometry. For the network architecture, fully connected layers are employed with 5 layers and 100 neurons per layer, and the hyperbolic tangent is used for activation functions [Raissi et al., 2019]. To minimize the loss function, we adopt L-BFGS optimizer with the number of maximum epochs equal to 5×10^5 . To evaluate the models, for each geometry, we choose $N_{test} = 20000$ points and calculate the error of the prediction on these testing points.

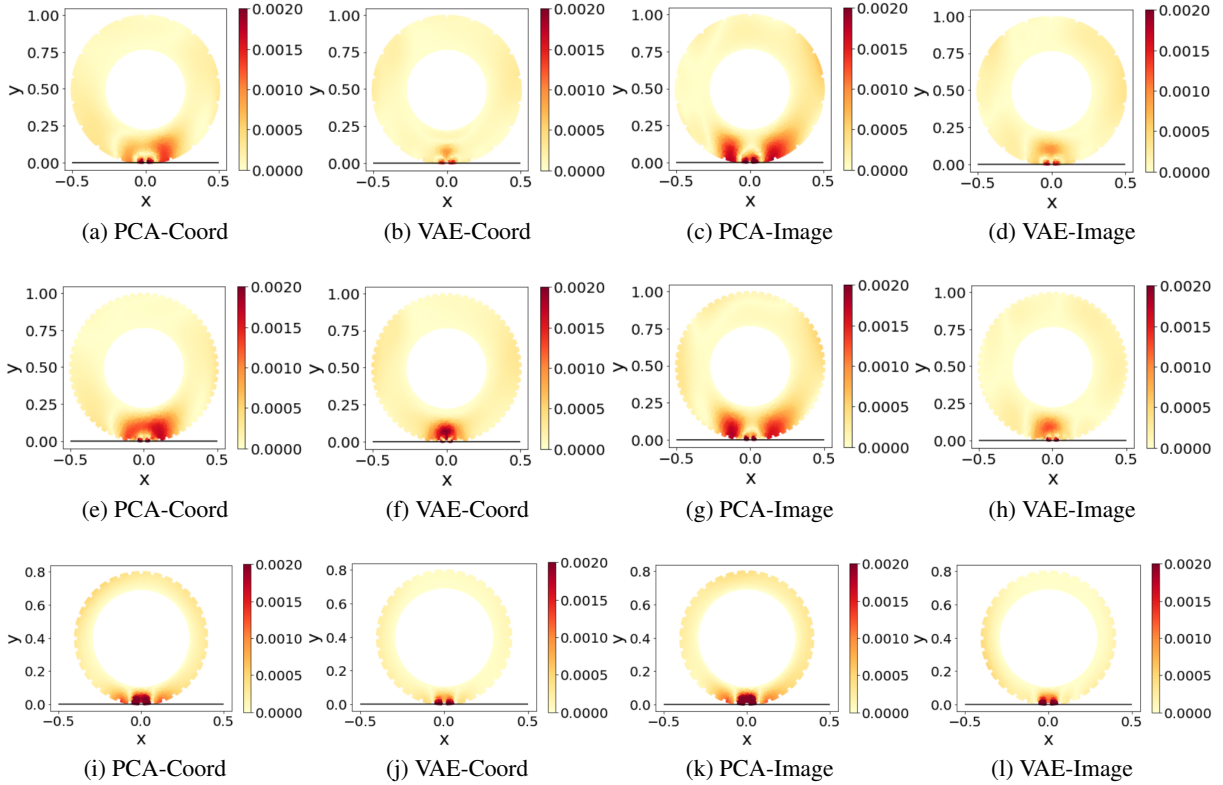


Figure 11: Visualization of the absolute error between the reference and the prediction GADEM approaches for a tire in the training set (a-d), first testing set (e-h), and second testing set (i-l).

Figure 11 illustrates the errors produced by different approaches of GADEM for a tire in the training, the first testing set, and the second testing set (ODD testing set). We see that the VAE-Coord provides the smallest errors for the displacement among all considered approaches. The prediction of the VAE-Coord approach for the displacement on different tires in the training and testing set is shown in Figure 12. We see that GADEM is able to predict accurately the solution for the displacement on different shapes of tire geometries. Figures 13 and 14 show the accuracy of GADEM for all geometries in the training and testing sets. Again, the methods using spatial coordinates (PCA-Coord and VAE-Coord) outperform the methods using images to represent the geometries. The VAE's approaches provide better

accuracy than the PCA's approaches. Among all methods, the VAE-Coord approach gives the best performance in terms of accuracy in both the training and testing sets.

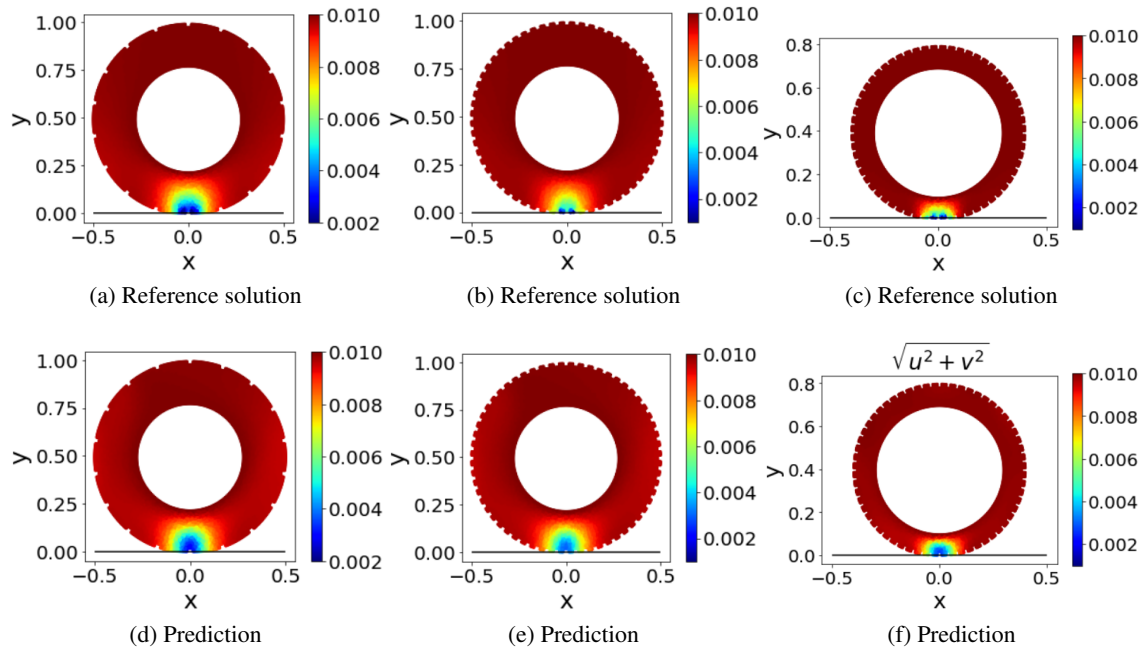


Figure 12: Visualization of the displacement $\|u\|$ for a tire in the training set (a)-(d), the first testing set (b)-(e), and the second testing set (c)-(f). The prediction is obtained by using GADEM with the VAE-Coord approach.

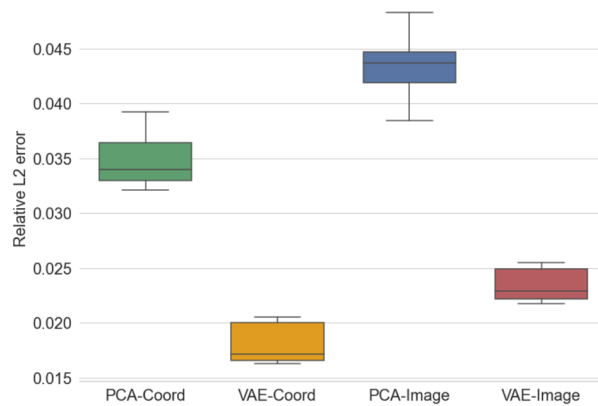


Figure 13: Performance for all geometries in the training data set.

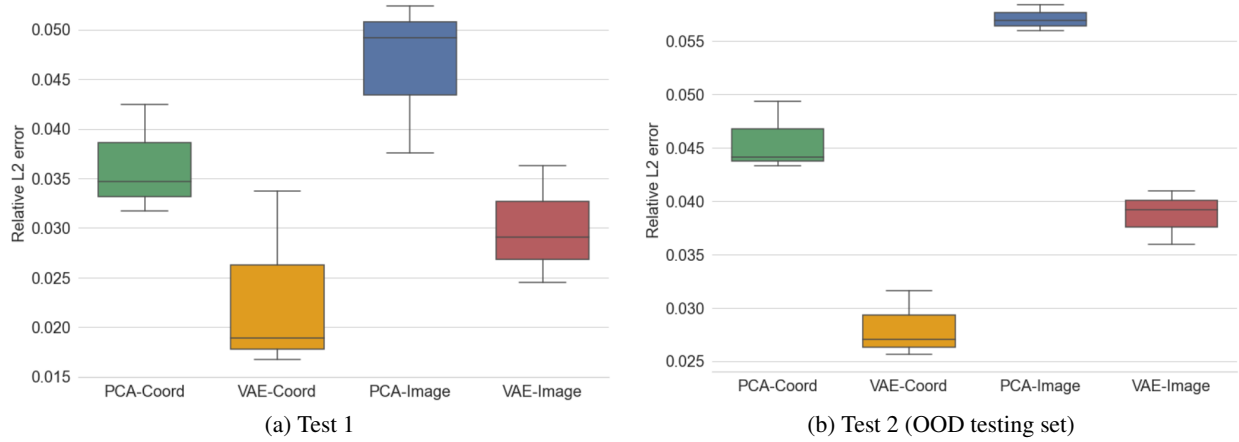


Figure 14: Performance on the testing data sets.

5.2.3 Enhance the accuracy with FBOAL

As the displacement of all the tires is only important when there is contact, we use FBOAL to infer the location of the training points to enhance the accuracy of GADEM at the contact zone. For the sake of comparison, we use the same initial training configuration as described in section 5.2.2. For the training, on each geometry, we take $N_j = 2500$ collocation points, which are randomly generated inside the domain, to minimize the energy. This leads to the total number of collocation points $N = 44 \times 2500 = 110000$. For the contact constraints, we take $N_c^j = 600$ points on the potential contact boundary of each geometry, which leads to the number of training points on contact zone $N_c = 6000$. For the training of FBOAL, we first train the network for $K = 500000$ iterations, and then after every $k = 100000$ iterations, we add and remove $m = 1\% \times N = 1100$ collocation points based on the quantity to minimize on all the training geometries $\{\Omega^j\}_{j=1}^G$. We also add and remove $m_c = 1\% \times N_C = 600$ points based on the quantity to minimize on all potential contact zones $\{\Omega_C^j\}_{j=1}^G$. Again, the values of these hyperparameters are chosen based on the conclusion of the work of Nguyen et al. [2023].

Figure 15 shows the loss function during the training process and the relative \mathcal{L}^2 errors on the testing points produced by GADEM with and without FBOAL. Again, when FBOAL effectuates the resampling, we observe the jumps in the loss function. Thus the loss functions produced by GADEM with FBOAL are less well minimized than the loss produced by GADEM without FBOAL (Figure 15a). However, the errors of the prediction on the testing points are significantly reduced by using GADEM with FBOAL (Figure 15b).

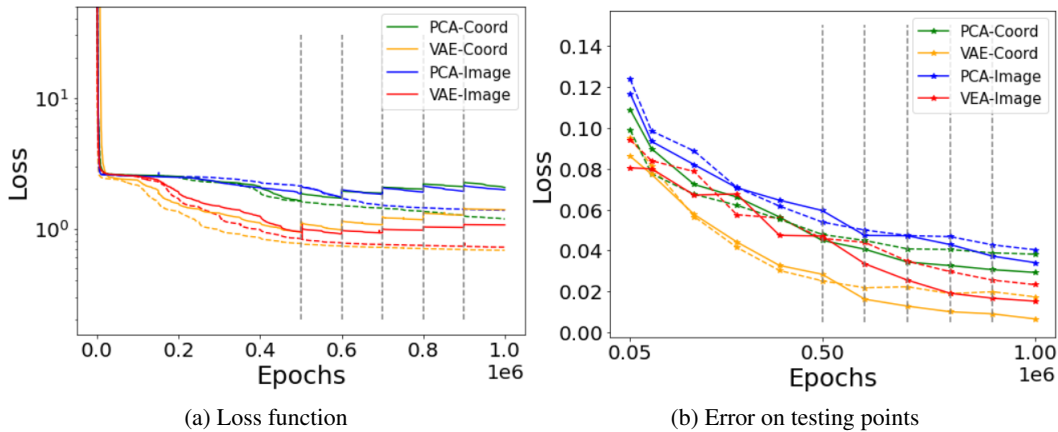


Figure 15: Loss function during the training process and the relative \mathcal{L}^2 errors on the testing points (average results of all geometries) produced by GADEM without FBOAL (dashed lines) and GADEM with FBOAL (solid lines). The gray lines indicate the instances where FBOAL effectuates the resampling.

		PCA-Coord	VAE-Coord	PCA-Image	VAE-Image
Train	W/o FBOAL	$3.56e-2 \pm 2.28e-3$	$1.95e-2 \pm 1.17e-3$	$4.43e-2 \pm 2.55e-3$	$2.33e-2 \pm 1.35e-3$
	With FBOAL	$1.41e-2 \pm 4.19e-3$	$1.02e-2 \pm 3.76e-3$	$3.13e-2 \pm 5.55e-3$	$1.63e-2 \pm 5.31e-3$
Test 1	W/o FBOAL	$3.63e-2 \pm 4.55e-3$	$2.31e-2 \pm 7.55e-3$	$4.63e-2 \pm 8.89e-3$	$2.99e-2 \pm 4.41e-3$
	With FBOAL	$2.66e-2 \pm 5.27e-3$	$1.94e-2 \pm 4.98e-3$	$3.44e-2 \pm 8.06e-3$	$2.17e-2 \pm 4.65e-3$
Test 2	W/o FBOAL	$4.55e-2 \pm 2.03e-3$	$2.80e-2 \pm 1.67e-3$	$5.71e-2 \pm 1.24e-3$	$3.86e-2 \pm 1.19e-3$
	With FBOAL	$4.28e-2 \pm 2.11e-3$	$2.49e-2 \pm 1.75e-3$	$5.56e-2 \pm 2.06e-3$	$3.49e-2 \pm 1.74e-3$

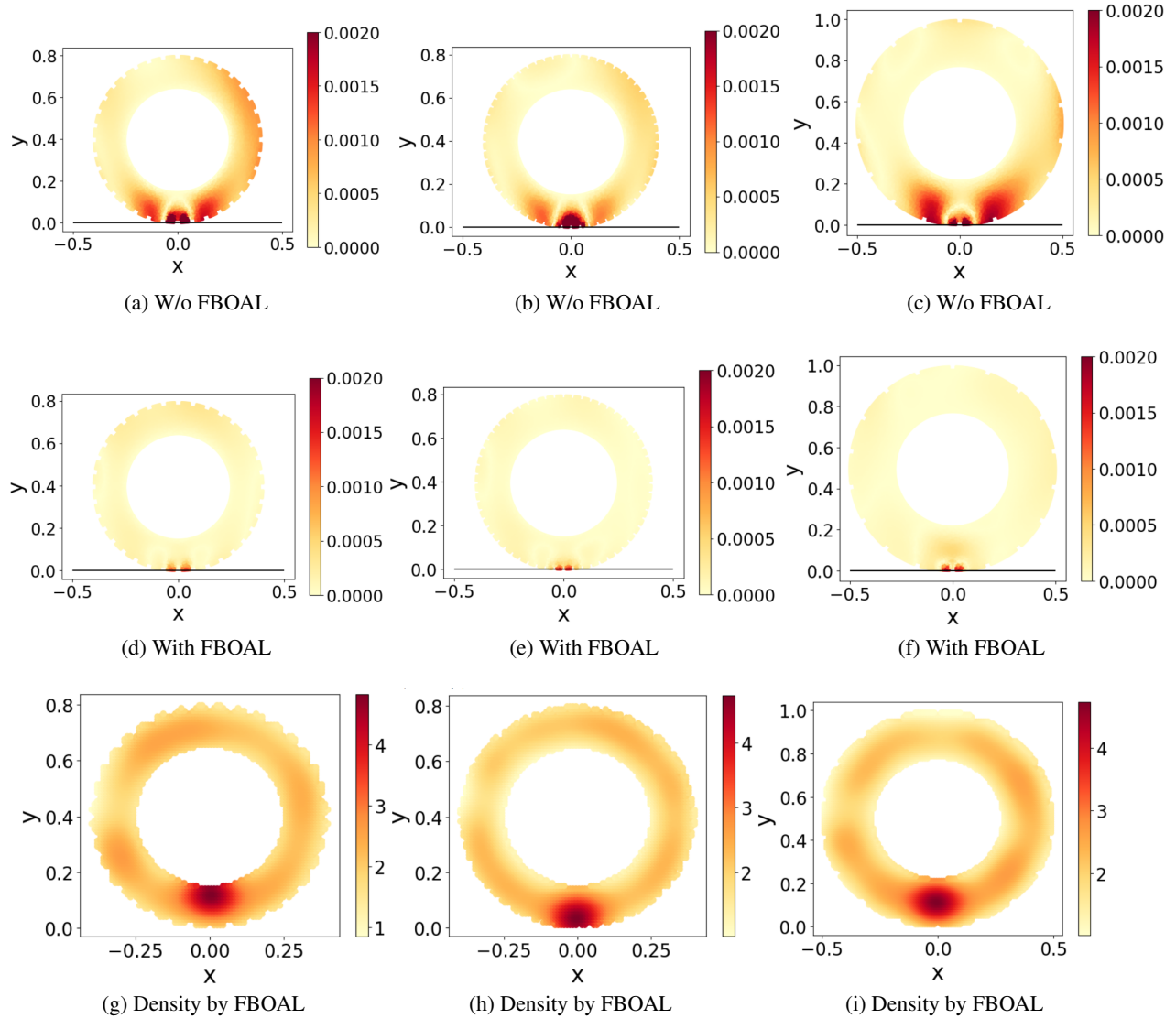
 Table 4: Relative \mathcal{L}^2 errors of all the approaches with and without using FBOAL.


Figure 16: Visualization of the absolute errors produced by GADEM with the PCA-Coord approaches without using FBOAL (a-c), with using FBOAL on the corresponding tires (d-f), and the density of collocation points after the training with FBOAL on the corresponding tires (g-i).

Figure 16 visualizes the errors with and without FBOAL, the density of collocation points after the training with FBOAL on different training geometries. We see that FBOAL adds many points close to the contact positions for all geometries. This is reasonable as the potential energy is important in this area. The errors near the contact area are significantly reduced by using FBOAL. Table 4 shows the relative \mathcal{L}^2 errors (average results of all the geometries) between the

reference solution and the prediction of GADEM approaches. The good results (errors smaller than 3%) are highlighted. Again, with the adaptive learning strategy FBOAL, we gain a huge accuracy compared to the classical approaches that fix the collocation points for the training data set. The same conclusion can be drawn for the testing sets.

6 Conclusion

In this study, we introduced the Geometry-Aware Deep Energy Method (GADEM) based on PINNs for the modeling of structural mechanics problems, which is capable of inferring the solution on different shapes of geometries. To represent the geometries, either boundary spatial coordinates or object images can be used. In the first phase of training, GADEM employs either parametric encoding or dimensionality reduction methods (PCA or VAE) to extract the geometric latent vectors. In the second phase, these latent vectors are considered as additional inputs of the model, and we minimize the potential energy of the systems over all the geometries in the loss function. We validate our proposed framework in an academic test case involving linear elasticity with various types of geometries. We then investigate the use of GADEM in a more realistic industrial problem of tire loading simulation. As far as our knowledge, this is the first time a physics-informed deep learning framework has been successfully applied to solve a contact mechanics problem involving hyperelastic materials. Through this work, GADEM has shown a great capability to predict the solution for different shapes of geometries using only one trained model. Consistently, using spatial coordinates to represent the geometries provides better accuracy than using images, and using the VAE for the encoding provides more accurate results when dealing with complex geometries than using the PCA. We also employed an adaptive learning strategy to infer the best location for the training collocation points in GADEM. With this method, it has been shown that the accuracy of GADEM can be further improved. Besides that, the idea of GADEM can be explored for solving other problems involving PDEs on different geometries.

It can be seen that there are many challenges and opportunities for further research. In this work, we only consider the cases where the boundary conditions are the same for all geometries. In the case where different boundary conditions are applied to different geometries, GADEM can also be employed. However, there will be a need to incorporate the geometries and boundary conditions to improve the performance of the model. Furthermore, one could employ GADEM for new design generation, that is, VAE could be used to generate new latent vectors corresponding to new geometries, and GADEM could be used to predict the solution on these whole new geometries. We aim to purchase these lines of research for future studies.

Acknowledgements

T.N.K. Nguyen is funded by Michelin and CEA through the Industrial Data Analytics and Machine Learning chair of ENS Paris-Saclay.

A About the of the PCA and VAE

A.1 Configuration and architecture

The architecture of the VAE models used in this work is described as follows:

- For the VAE on the spatial coordinates: in the encoder, we use five 1D convolutional layers of size [32, 64, 128, 256, 512], followed by three fully connected layers of size [256, 256, 256] with ReLU activation. In the decoder, we use three fully connected layers of size [256, 256, 256].
- For the VAE on the images: in the encoder, we use two 2D convolutional layers in sequential order, ReLU activation with 3x3 kernel sizes, and 32, 64 and filters, followed by two fully connected layers of size [16, 5] (where 5 represents the size of latent vector). In the decoder,

To minimize the loss function in the VAE, we adopt Adam optimizer with the learning rate decay strategy, which is proven to be very efficient in training deep learning models [You et al., 2019]. The results are obtained with 1,000 epochs with the learning rate $lr = 10^{-3}$, followed by 1,000 epochs with the learning rate $lr = 10^{-4}$ and 1,000 epochs with $lr = 10^{-5}$.

A.2 Performance on the academic case

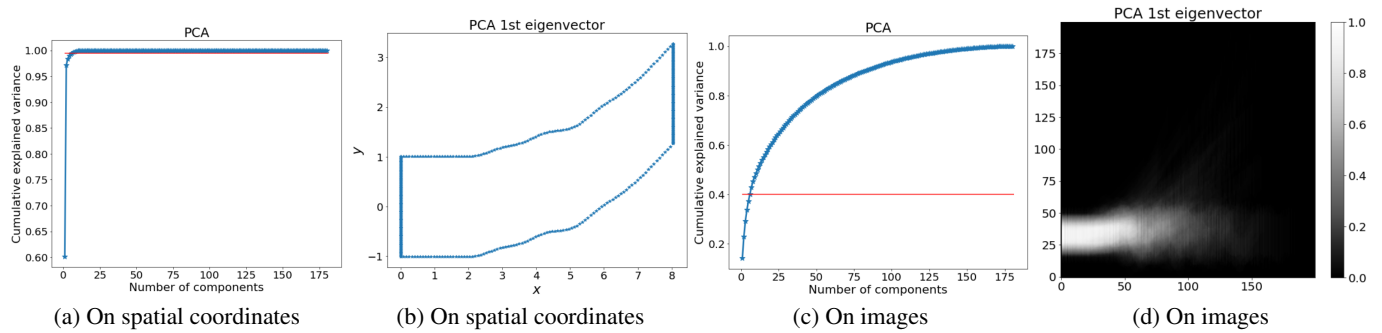


Figure 17: Visualization for the PCA: Cumulative explained variance and first eigenvector.

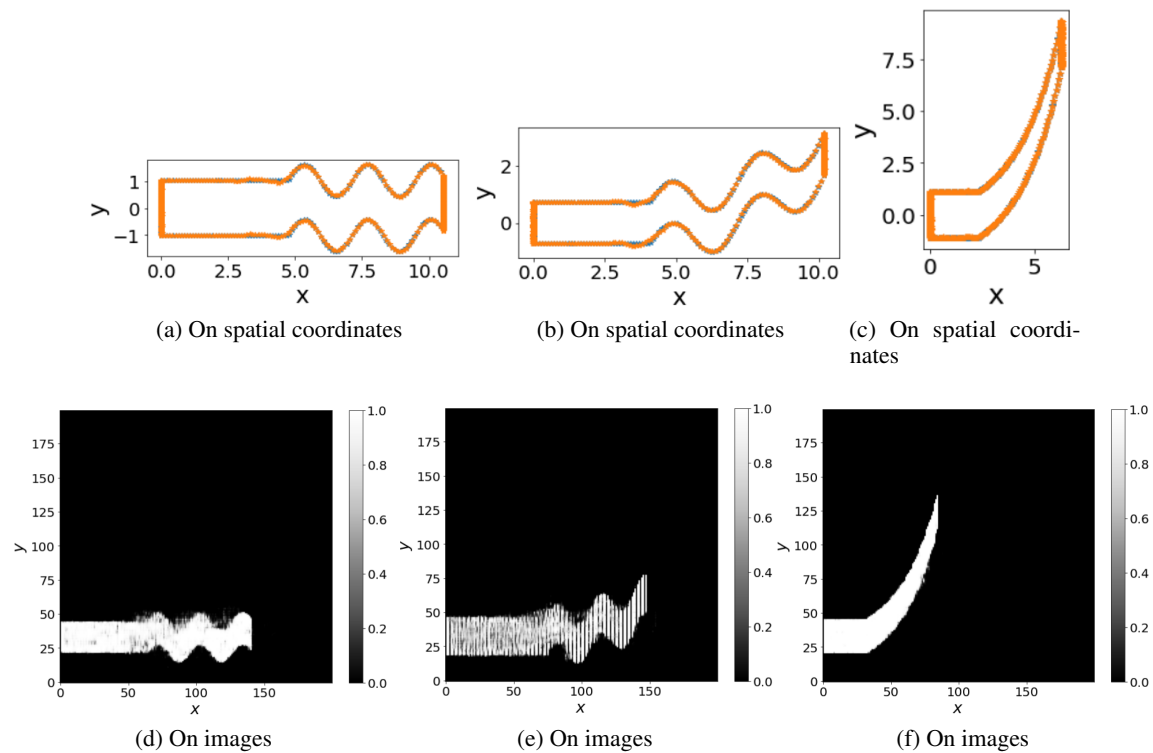


Figure 18: Reconstruction of the VAE for different beams.

To visualize the geometric latent vectors in a 2D space, we employ the TSNE technique (t-distributed Stochastic Neighbor Embedding [Van der Maaten and Hinton, 2008]), which is a nonlinear dimensionality reduction method for embedding high-dimensional data in a 2D or 3D space for visualization. Figure 19 shows the latent vectors in the reduced TSNE space. For the parametric encoding (Figure 19a), as this method only encodes the parameters l, d, l_1, p_1, p_2 , not the sinus, polynomial, or exponential information, we see that this approach only distinguishes well the training and testing sets when the learning intervals of the parameters are different (e.g. the latent vector of the second test located differently from other sets). For the PCA-Coord and VAE-Coord approaches (Figures 19b and 19c), we see that the latent vectors of the first and second training sets are well-distinguished. The latent vectors of the first test (where the geometries have the same shapes and learning intervals as the training set) are located within the space between the training sets, while the second test (where the geometries have the same shapes but different learning intervals as the training set) are located outside this space. For the third set, as the geometry shapes in this set are a

combination of the two training sets, the latent vector of this set lies between the space of the first training set and the second training set. For the fourth test, although this test set composes new geometries of exponential shapes, these geometries have very similar shapes to the polynomial training set (second training set). Thus we see that the latent vector of this set lies close to the second training set. A similar interpretation can be obtained for the PCA-Image and VAE-Image approaches (Figures 19d and 19e), however, the difference between the training and testing sets can not clearly observed.

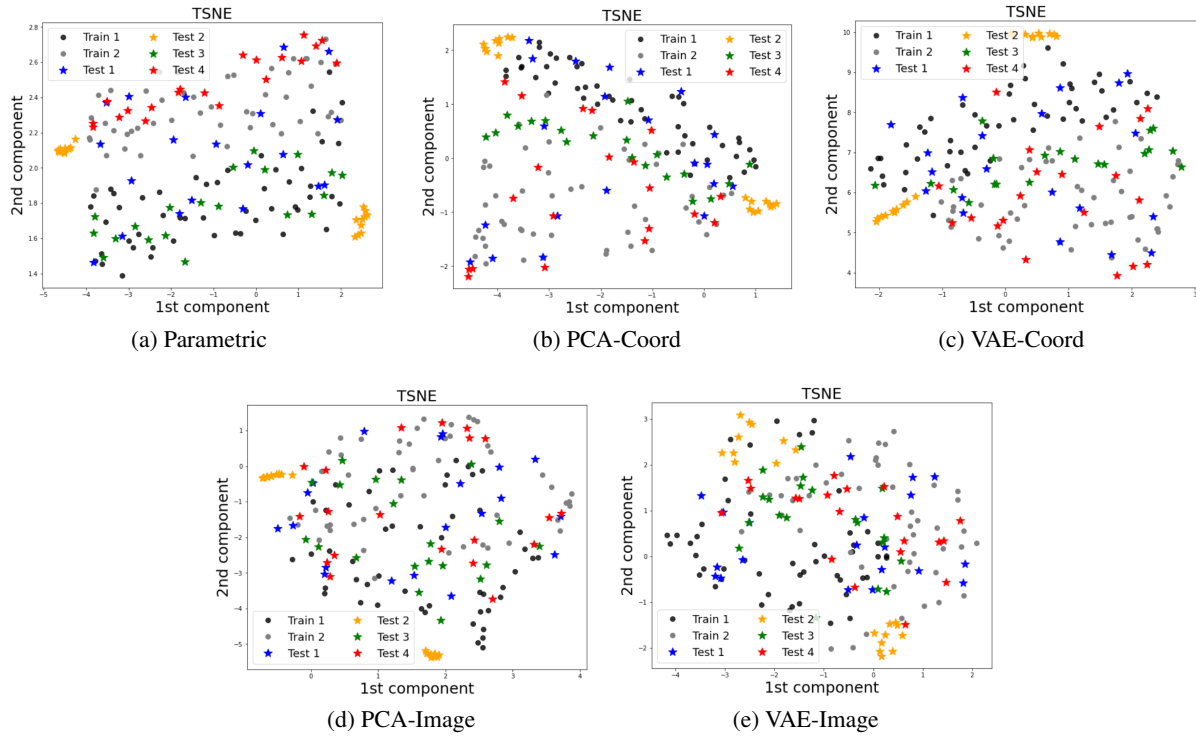


Figure 19: Visualization of the latent vectors in the reduced space by TSNE.

A.3 Performance on the tire loading simulation

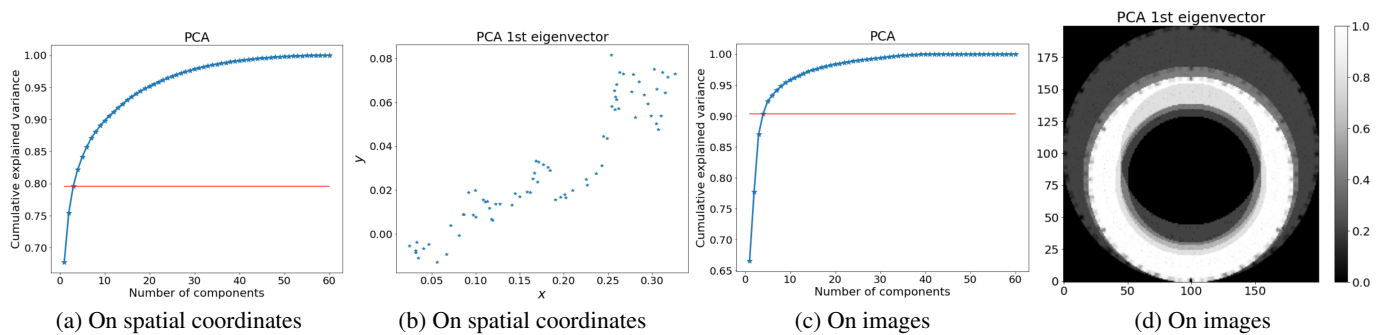


Figure 20: Visualization for the PCA: Cumulative explained variance and first eigenvector.

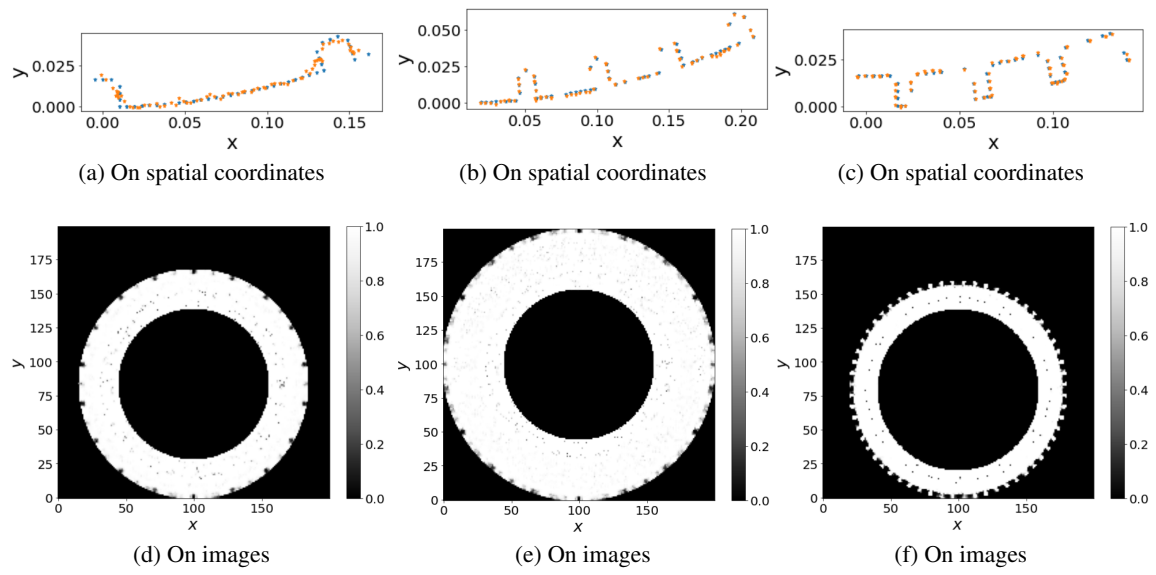


Figure 21: Reconstruction of the VAE for different tires.

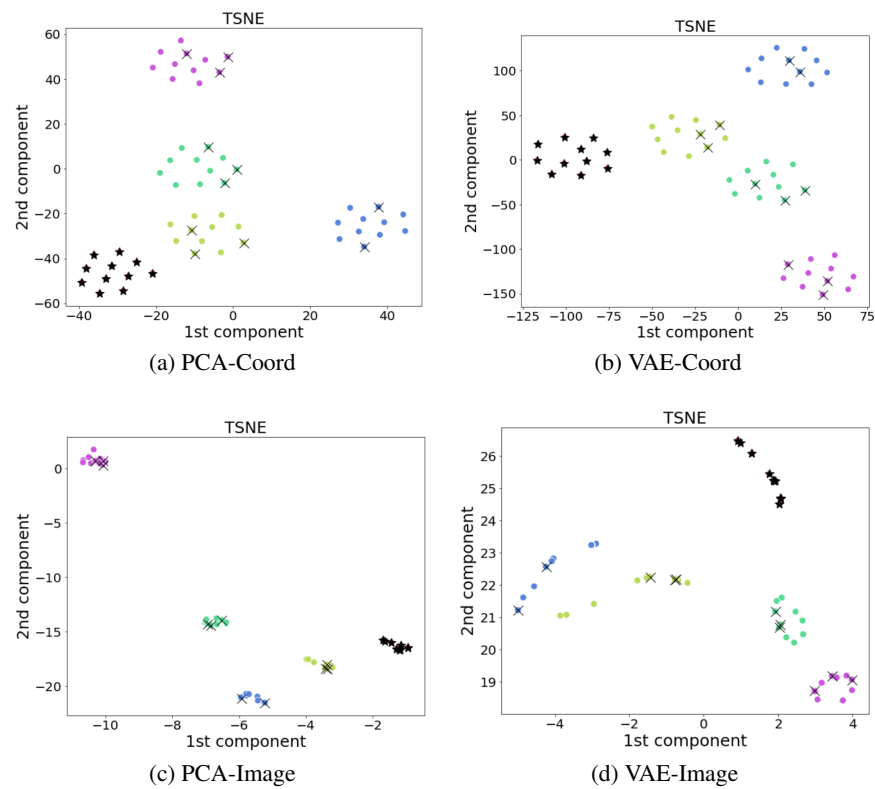


Figure 22: Visualization of latent vectors with $k_z = 5$ of different dimensionality reduction methods by T-SNE technique. Each color represents each main group of geometries. The 'x' symbol denotes the tires on the first testing data set. The '*' symbol denotes the tires on the second testing data set.

Figure 22 illustrates the latent vectors of the PCA and VAE with $k_z = 5$ in reduced space produced by the T-SNE for the visualization. We see that the latent vectors of five main classes of tire geometries are grouped well by all reduction methods, and the differences between each class are well-observed.

B Results in tire loading simulation when choosing another OOD testing set

We provide the error of GADEM approaches when choosing another group rather than the fifth group as the OOD testing set. The following results are obtained with the vanilla GADEM (*i.e.* without using FBOAL to enhance the accuracy).

Figures 23, 24, 25, 26 represent the box plots of relative errors between the prediction of GADEM and the reference solution when taking the group 1, 2, 3, 4 as the OOD testing set, respectively. We see that, with all cases, we obtain the same conclusion, *i.e.*, the GADEM approaches with VAE always perform better than GADEM approaches with PCA. And using the spatial coordinates provides better accuracy than using images.

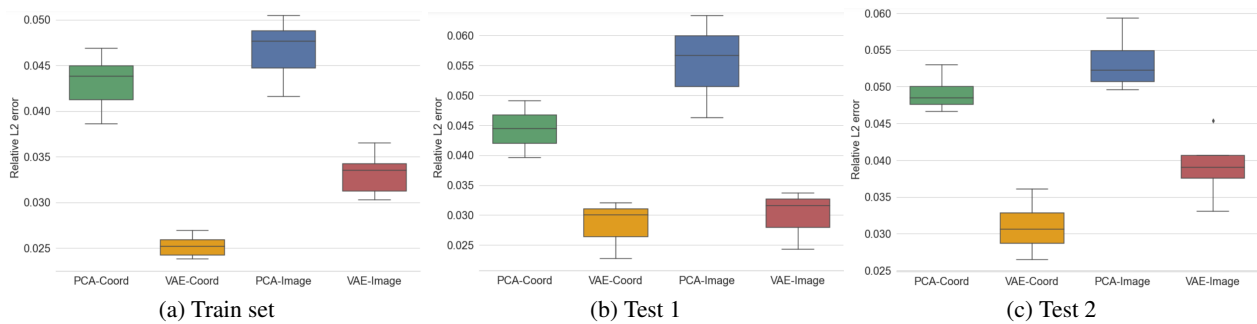


Figure 23: Group 1 as OOD set: Performance on training and testing data sets.

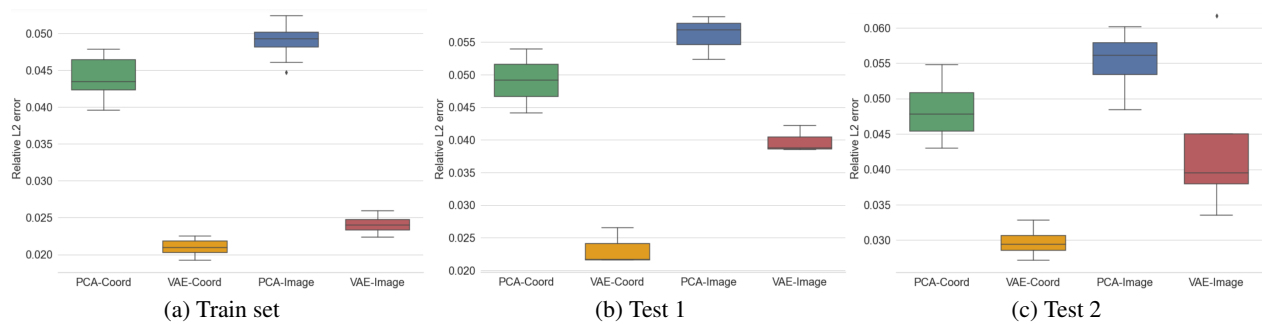


Figure 24: Group 2 as OOD set: Performance on training and testing data sets.

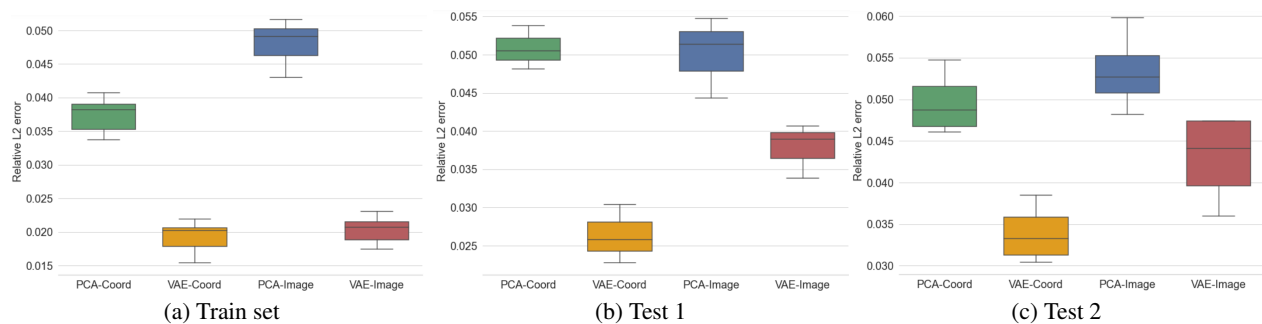


Figure 25: Group 3 as OOD set: Performance on training and testing data sets.

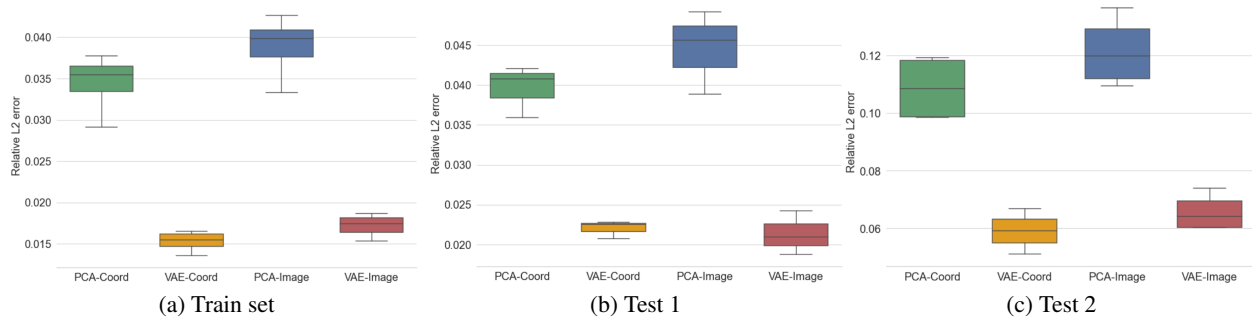


Figure 26: Group 4 as OOD set: Performance on training and testing data sets.

References

- Diab W Abueidda, Seid Koric, Erman Guleryuz, and Nahil A Sobh. Enhanced physics-informed neural networks for hyperelasticity. *International Journal for Numerical Methods in Engineering*, 124(7):1585–1601, 2023.
- William F Ames. *Numerical methods for partial differential equations*. Academic press, 2014.
- David Amsallem. *Interpolation on manifolds of CFD-based fluid and finite element-based structural reduced-order models for on-line aeroelastic predictions*. Stanford University, 2010.
- Amirhossein Arzani, Jian-Xun Wang, and Roshan M D’Souza. Uncovering near-wall blood flow from sparse data with physics-informed neural networks. *Physics of Fluids*, 33(7), 2021.
- Atilim Gunes Baydin, Barak A Pearlmutter, Alexey Andreyevich Radul, and Jeffrey Mark Siskind. Automatic differentiation in machine learning: a survey. *Journal of machine learning research*, 18, 2018.
- Jens Berg and Kaj Nyström. A unified deep artificial neural network approach to partial differential equations in complex geometries. *Neurocomputing*, 317:28–41, 2018.
- Scott Cameron, Arnú Pretorius, and Stephen Roberts. Nonparametric boundary geometry in physics informed deep learning. *Advances in Neural Information Processing Systems*, 36, 2024.
- Charul Chadha, Diab Abueidda, Seid Koric, Erman Guleryuz, and Iwona Jasiuk. Optimizing hyperparameters and architecture of deep energy method. 2022.
- Qijing Chen, Qi Ye, Weiqi Zhang, He Li, and Xiaoning Zheng. Tgm-nets: A deep learning framework for enhanced forecasting of tumor growth by integrating imaging and modeling. *Engineering Applications of Artificial Intelligence*, 126:106867, 2023.
- Yuyao Chen, Lu Lu, George Em Karniadakis, and Luca Dal Negro. Physics-informed neural networks for inverse problems in nano-optics and metamaterials. *Optics express*, 28(8):11618–11633, 2020.
- Arka Daw, Jie Bu, Sifan Wang, Paris Perdikaris, and Anuj Karpatne. Rethinking the importance of sampling in physics-informed neural networks. *arXiv preprint arXiv:2207.02338*, 2022.
- JP De SR Gago, Donald W Kelly, Olgierd C Zienkiewicz, and I Babuska. A posteriori error analysis and adaptive processes in the finite element method: Part ii—adaptive mesh refinement. *International journal for numerical methods in engineering*, 19(11):1621–1656, 1983.
- Zhiwei Fang. A high-efficient hybrid physics-informed neural networks based on convolutional neural network. *IEEE Transactions on Neural Networks and Learning Systems*, 33(10):5514–5526, 2021.
- André Fortin and André Garon. *Les éléments finis: de la théorie à la pratique*. Université Laval, 2011.
- Jan N Fuhg and Nikolaos Bouklas. The mixed deep energy method for resolving concentration features in finite strain hyperelasticity. *Journal of Computational Physics*, 451:110839, 2022.
- Han Gao, Luning Sun, and Jian-Xun Wang. Phygeonet: Physics-informed geometry-adaptive convolutional neural networks for solving parameterized steady-state pdes on irregular domain. *Journal of Computational Physics*, 428:110079, 2021.
- Ehsan Haghghat, Maziar Raissi, Adrian Moure, Hector Gomez, and Ruben Juanes. A physics-informed deep learning framework for inversion and surrogate modeling in solid mechanics. *Computer Methods in Applied Mechanics and Engineering*, 379:113741, 2021.

- Ameya D Jagtap and George E Karniadakis. Extended physics-informed neural networks (xpinns): A generalized space-time domain decomposition based deep learning framework for nonlinear partial differential equations. In *AAAI spring symposium: MLPS*, volume 10, 2021.
- Ameya D Jagtap, Kenji Kawaguchi, and George Em Karniadakis. Locally adaptive activation functions with slope recovery for deep and physics-informed neural networks. *Proceedings of the Royal Society A*, 476(2239):20200334, 2020a.
- Ameya D Jagtap, Kenji Kawaguchi, and George Em Karniadakis. Adaptive activation functions accelerate convergence in deep and physics-informed neural networks. *Journal of Computational Physics*, 404:109136, 2020b.
- Ameya D Jagtap, Yeonjong Shin, Kenji Kawaguchi, and George Em Karniadakis. Deep kronecker neural networks: A general framework for neural networks with adaptive activation functions. *Neurocomputing*, 468:165–180, 2022.
- Ian T Jolliffe. *Principal component analysis for special types of data*. Springer, 2002.
- George Em Karniadakis, Ioannis G Kevrekidis, Lu Lu, Paris Perdikaris, Sifan Wang, and Liu Yang. Physics-informed machine learning. *Nature Reviews Physics*, 3(6):422–440, 2021.
- Ali Kashefi and Tapan Mukerji. Physics-informed pointnet: A deep learning solver for steady-state incompressible flows and thermal fields on multiple sets of irregular geometries. *Journal of Computational Physics*, 468:111510, 2022.
- Ehsan Kharazmi, Zhongqiang Zhang, and George Em Karniadakis. Variational physics-informed neural networks for solving partial differential equations. *arXiv preprint arXiv:1912.00873*, 2019.
- Houari Boumediène Khenous, Julien Pommier, and Yves Renard. Hybrid discretization of the signorini problem with coulomb friction. theoretical aspects and comparison of some numerical solvers. *Applied Numerical Mathematics*, 56(2):163–192, 2006.
- Diederik P Kingma, Max Welling, et al. An introduction to variational autoencoders. *Foundations and Trends® in Machine Learning*, 12(4):307–392, 2019.
- Georgios Kissas, Yibo Yang, Eileen Hwuang, Walter R Witschey, John A Detre, and Paris Perdikaris. Machine learning in cardiovascular flows modeling: Predicting arterial blood pressure from non-invasive 4d flow mri data using physics-informed neural networks. *Computer Methods in Applied Mechanics and Engineering*, 358:112623, 2020.
- Seung-Woo Lee, Chien Truong-Quoc, Youngmin Ro, and Do-Nyun Kim. Adversarial deep energy method for solving saddle point problems involving dielectric elastomers. *Computer Methods in Applied Mechanics and Engineering*, 421:116825, 2024.
- Wei Li, Martin Z Bazant, and Juner Zhu. A physics-guided neural network framework for elastic plates: Comparison of governing equations-based and energy-based approaches. *Computer Methods in Applied Mechanics and Engineering*, 383:113933, 2021.
- Zongyi Li, Nikola Kovachki, Kamyar Azizzadenesheli, Burigede Liu, Kaushik Bhattacharya, Andrew Stuart, and Anima Anandkumar. Fourier neural operator for parametric partial differential equations. *arXiv preprint arXiv:2010.08895*, 2020.
- Zongyi Li, Daniel Zhengyu Huang, Burigede Liu, and Anima Anandkumar. Fourier neural operator with learned deformations for pdes on general geometries. *Journal of Machine Learning Research*, 24(388):1–26, 2023.
- Zeyu Liu, Yantao Yang, and Qing-Dong Cai. Solving differential equation with constrained multilayer feedforward network. *arXiv preprint arXiv:1904.06619*, 2019.
- Anders Logg, Kent-Andre Mardal, and Garth Wells. *Automated solution of differential equations by the finite element method: The FEniCS book*, volume 84. Springer Science & Business Media, 2012.
- Lu Lu, Xuhui Meng, Zhiping Mao, and George Em Karniadakis. Deepxde: A deep learning library for solving differential equations. *SIAM Review*, 63(1):208–228, 2021a.
- Lu Lu, Raphael Pestourie, Wenjie Yao, Zhicheng Wang, Francesc Verdugo, and Steven G Johnson. Physics-informed neural networks with hard constraints for inverse design. *SIAM Journal on Scientific Computing*, 43(6):B1105–B1132, 2021b.
- Levi McClenny and Ulisses Braga-Neto. Self-adaptive physics-informed neural networks using a soft attention mechanism. *arXiv preprint arXiv:2009.04544*, 2020.
- Ben Moseley, Andrew Markham, and Tarje Nissen-Meyer. Finite basis physics-informed neural networks (fbpinns): a scalable domain decomposition approach for solving differential equations. *Advances in Computational Mathematics*, 49(4):62, 2023.

- Thi Nguyen Khoa Nguyen, Thibault Dairay, Raphaël Meunier, and Mathilde Mougeot. Physics-informed neural networks for non-newtonian fluid thermo-mechanical problems: An application to rubber calendaring process. *Engineering Applications of Artificial Intelligence*, 114:105176, 2022.
- Thi Nguyen Khoa Nguyen, Thibault Dairay, Raphaël Meunier, Christophe Millet, and Mathilde Mougeot. Fixed-budget online adaptive learning for physics-informed neural networks. towards parameterized problem inference. In *International Conference on Computational Science*, pages 453–468. Springer, 2023.
- Vien Minh Nguyen-Thanh, Xiaoying Zhuang, and Timon Rabczuk. A deep energy method for finite deformation hyperelasticity. *European Journal of Mechanics-A/Solids*, 80:103874, 2020.
- Vien Minh Nguyen-Thanh, Cosmin Anitescu, Naif Alajlan, Timon Rabczuk, and Xiaoying Zhuang. Parametric deep energy approach for elasticity accounting for strain gradient effects. *Computer Methods in Applied Mechanics and Engineering*, 386:114096, 2021.
- Jan Oldenburg, Finja Borowski, Alper Öner, Klaus-Peter Schmitz, and Michael Stiehm. Geometry aware physics informed neural network surrogate for solving navier–stokes equation (gapinn). *Advanced Modeling and Simulation in Engineering Sciences*, 9(1):8, 2022.
- Guofei Pang, Lu Lu, and George Em Karniadakis. fpinns: Fractional physics-informed neural networks. *SIAM Journal on Scientific Computing*, 41(4):A2603–A2626, 2019.
- Panayiotis Papadopoulos and Robert L Taylor. A mixed formulation for the finite element solution of contact problems. *Computer Methods in Applied Mechanics and Engineering*, 94(3):373–389, 1992.
- Wei Peng, Weien Zhou, Xiaoya Zhang, Wen Yao, and Zheliang Liu. Rang: A residual-based adaptive node generation method for physics-informed neural networks. *arXiv preprint arXiv:2205.01051*, 2022.
- Alfio Quarteroni and Alberto Valli. *Numerical approximation of partial differential equations*, volume 23. Springer Science & Business Media, 2008.
- Christopher Rackauckas, Yingbo Ma, Julius Martensen, Collin Warner, Kirill Zubov, Rohit Supekar, Dominic Skinner, Ali Ramadhan, and Alan Edelman. Universal differential equations for scientific machine learning. *arXiv preprint arXiv:2001.04385*, 2020.
- Maziar Raissi, Paris Perdikaris, and George E Karniadakis. Physics-informed neural networks: A deep learning framework for solving forward and inverse problems involving nonlinear partial differential equations. *Journal of Computational Physics*, 378:686–707, 2019.
- Pu Ren, Chengping Rao, Yang Liu, Jian-Xun Wang, and Hao Sun. Phycrnet: Physics-informed convolutional-recurrent network for solving spatiotemporal pdes. *Computer Methods in Applied Mechanics and Engineering*, 389:114399, 2022.
- Y Renard and J Pommier. Getfem finite element library. URL: <http://home.gna.org/getfem>, 2007.
- Tarik Sahin, Max von Danwitz, and Alexander Popp. Solving forward and inverse problems of contact mechanics using physics-informed neural networks. *arXiv preprint arXiv:2308.12716*, 2023.
- Esteban Samaniego, Cosmin Anitescu, Somdatta Goswami, Vien Minh Nguyen-Thanh, Hongwei Guo, Khader Hamdia, X Zhuang, and T Rabczuk. An energy approach to the solution of partial differential equations in computational mechanics via machine learning: Concepts, implementation and applications. *Computer Methods in Applied Mechanics and Engineering*, 362:112790, 2020.
- Louis Serrano, Lise Le Boudec, Armand Kassai Koupaï, Thomas X Wang, Yuan Yin, Jean-Noël Vittaut, and Patrick Gallinari. Operator learning with neural fields: Tackling pdes on general geometries. *Advances in Neural Information Processing Systems*, 36, 2024.
- Khemraj Shukla, Ameya D Jagtap, James L Blackshire, Daniel Sparkman, and George Em Karniadakis. A physics-informed neural network for quantifying the microstructural properties of polycrystalline nickel using ultrasound data: A promising approach for solving inverse problems. *IEEE Signal Processing Magazine*, 39(1):68–77, 2021.
- Erik Laurin Strelow, Alf Gerisch, Jens Lang, and Marc E Pfetsch. Physics informed neural networks: A case study for gas transport problems. *Journal of Computational Physics*, 481:112041, 2023.
- Laurens Van der Maaten and Geoffrey Hinton. Visualizing data using t-sne. *Journal of machine learning research*, 9(11), 2008.
- Sifan Wang, Yujun Teng, and Paris Perdikaris. Understanding and mitigating gradient pathologies in physics-informed neural networks. *arXiv preprint arXiv:2001.04536*, 2020a.
- Sifan Wang, Xinling Yu, and Paris Perdikaris. When and why pinns fail to train: A neural tangent kernel perspective. *arXiv preprint arXiv:2007.14527*, 2020b.

- Sifan Wang, Shyam Sankaran, and Paris Perdikaris. Respecting causality is all you need for training physics-informed neural networks. *arXiv preprint arXiv:2203.07404*, 2022.
- Chenxi Wu, Min Zhu, Qinyang Tan, Yadhu Kartha, and Lu Lu. A comprehensive study of non-adaptive and residual-based adaptive sampling for physics-informed neural networks. *Computer Methods in Applied Mechanics and Engineering*, 403:115671, 2023.
- Liu Yang, Xuhui Meng, and George Em Karniadakis. B-pinns: Bayesian physics-informed neural networks for forward and inverse pde problems with noisy data. *Journal of Computational Physics*, 425:109913, 2021.
- Kaichao You, Mingsheng Long, Jianmin Wang, and Michael I Jordan. How does learning rate decay help modern neural networks? *arXiv preprint arXiv:1908.01878*, 2019.
- Bing Yu et al. The deep ritz method: a deep learning-based numerical algorithm for solving variational problems. *Communications in Mathematics and Statistics*, 6(1):1–12, 2018.
- Shaojie Zeng, Zong Zhang, and Qingsong Zou. Adaptive deep neural networks methods for high-dimensional partial differential equations. *Journal of Computational Physics*, 463:111232, 2022.